

The Monge-Ampère trajectory correction for semi-Lagrangian schemes

Jean-Francois Cossette^{a,*}

^a*Université de Montréal, Montréal, Canada*

Piotr K. Smolarkiewicz^b

^b*European Centre for Medium-Range Weather Forecasts, Reading, UK*

Paul Charbonneau^c

^c*Université de Montréal, Montréal, Canada*

Abstract

Requiring that numerical estimates of the flow trajectories comply with the fundamental Euler expansion formula that governs the evolution of a volume of fluid leads to a second-order nonlinear Monge-Ampère partial differential equation (MAE). In [Cossette and Smolarkiewicz, *Comput Fluids* **46**, 180 (2011); CS11], a numerical algorithm based on solving the MAE with an inexact Newton-Krylov solver has been developed and used to correct standard estimates of the departure points of flow trajectories provided by a classical semi-Lagrangian scheme in the context of an incompressible fluid. Here we extend the theoretical analysis of the elemental rotational and deformational motions presented in [CS11]. In particular, closed-form analytic solutions are derived for both cases that serve to illustrate the mechanics of the enhanced trajectory scheme and to address the issues of existence and uniqueness. Scalar advection shows that the MA correction improves mass conservation substantially by suppressing anomalous fluid contraction. The impact of the MA correction on complex flows is studied in the framework of an ideal magneto-fluid in which the formation of current sheets leads to topological changes and reconnection of field lines. The use of the MA correction improves the numerical stability of the solutions and prevents trajectory intersections as well as the spurious growth of the magnetic energy. 2D and 3D examples are presented and the computational performance of the solver is documented.

Key words: Semi-Lagrangian schemes, incompressible flows, Monge-Ampere equation, Nonlinear equations, Newton-Krylov methods, passive advection, magnetohydrodynamics, magnetic reconnection

PACS:

1 INTRODUCTION

Discretizing analytical fluid PDEs into a form that is amenable to numerical integration has to take into account the key aspects of stability, consistency, accuracy and efficiency. Depending upon the physical application and the aim of the user, specific features that are inherent to the analytical model may or may not be incorporated into the architecture of the numerical algorithm. Such properties are, for instance, conservation laws, monotonicity, positive-definiteness of the scheme, total-variation diminishing constraints, or some form of compatibility [54]. In the brief proceedings paper [15], the Monge-Ampère (hereafter, MA) trajectory correction for semi-Lagrangian (SL) integration schemes was introduced as a means to enforce a type of compatibility based on the Lagrangian form of the mass continuity equation in the context of incompressible fluids. The execution of the MA correction requires solving a diagnostic nonlinear second-order PDE, the Monge-Ampère equation (MAE), to some approximation at each model time step. To interpret the MA correction in physical terms, we developed in [15] its theoretical analysis for elemental rotational and deformational motions. Here, we extend this analysis by providing closed-form analytic solutions for both elemental flows. These solutions illustrate the mechanics of the trajectory corrections and substantiate the arguments on the solution existence and uniqueness. The impact of the enhancement on scalar advection is revisited and its performance in the context of complex flows is assessed using a problem of relaxation to equilibrium in the ideal classical magnetohydrodynamical (MHD) approximation. What follows briefly summarizes the framework of SL methods before introducing the MA correction.

SL discretization schemes arise from a path integration

$$\psi(\mathbf{x}, t) = \psi(\mathbf{x}_0, t_0) + \int_T R dt \quad (1)$$

of a Lagrangian evolution equation

$$\frac{d\psi}{dt} = R, \quad (2)$$

in which d/dt denotes the total derivative along the flow trajectory $T : (\mathbf{x}_0, t_0) \rightarrow (\mathbf{x}_1, t)$, ψ is an arbitrary intensive fluid variable (e.g., temperature, chemical concentration or velocity component), and R symbolizes the associated right-hand-side (e.g., heat sources, chemical reactions, or pressure gradient force, respectively). Assuming the availability of ψ at all grid points \mathbf{x}_i at the instant t_0 , advancing the solution to $t = t_0 + \Delta t$ invokes three distinct steps.

* Corresponding Author.

Email address: `cossette@astro.umontreal.ca` (Jean-Francois Cossette).

First, trajectories arriving at the grid points \mathbf{x}_i at t are evaluated backward by approximating the path integral

$$\mathbf{x}_0 = \mathbf{x}_i - \int_{t_0}^t \mathbf{v}(\mathbf{x}(\tau), \tau) d\tau , \quad (3)$$

of the kinematic relation $d\mathbf{x}/dt = \mathbf{v}$. Second, the advected dependent variable $\psi(\mathbf{x}_i, t_0)$ is mapped to the set of the departure points $\psi(\mathbf{x}_i, t_0) \rightarrow \psi(\mathbf{x}_0, t_0)$ by means of interpolation. Third, contributions from forcings are accounted for as integrals along the trajectories [70,62,24,58,61].

SL methods are widely acknowledged for being superior in computational efficiency and stability relative to Eulerian schemes since they are not subject to the CFL condition. A major drawback of the classical SL approach is its lack of mass conservation, although improvements exist and are still being explored [69,72,60,39]. Many applications of SL schemes are found in numerical weather prediction (e.g. see [60] and references therein) and in the modelling of plasma dynamics, e.g. [42,28].

Intimately linked to the Lagrangian formulation of fluid mechanics is the interpretation of flows in terms of a space-time continuum, where the volume of fluid elements evolves in accordance with the *Euler expansion formula*

$$\frac{d \ln J}{dt} = \nabla \cdot \mathbf{v} , \quad (4)$$

with $J := \det(\partial\mathbf{x}/\partial\mathbf{x}_0)$ denoting the flow Jacobian [12,67]. The flow Jacobian has the interpretation of the ratio of final (evolved) to initial infinitesimal fluid parcel volumes (e.g. see [38], chapter I.14). Together with the evolutionary form of the mass continuity equation

$$\frac{d\rho}{dt} = -\rho \nabla \cdot \mathbf{v} , \quad (5)$$

the Euler formula (4) constitutes the base of the Lagrangian form of the mass conservation law

$$\rho(\mathbf{x}_i, t) = \hat{J}\rho(\mathbf{x}_0, t_0), \quad (6)$$

where $\hat{J} \equiv J^{-1} = \det(\partial\mathbf{x}_0/\partial\mathbf{x})$ is the inverse flow Jacobian [46]. Consequently, truncation errors in the evaluation of the departure points induce errors in the flow Jacobian, and so the compatibility of discrete counterparts of the integrals (1) and (3) with (6) is not ensured. This contrasts with Eulerian finite-volume methods, in which advecting velocities most often comply with the discrete mass continuity. In particular, for incompressible fluids the volume of each fluid element remains constant, upon which the relation

$$\hat{J} = 1 \quad (7)$$

becomes a necessary condition for the scheme’s compatibility. We wish to emphasize that (7) alone is not sufficient to ensure the compatibility since it does not take into account the remapping step, which also participates in the numerical realization of (6). To the authors’ knowledge, the extent to which both aspects affect the flow physics remains an open question. In this paper, we shall focus on the Lagrangian aspect of the compatibility, namely (7), and examine the impact of incompatible integrations on the observed flow features.

Specifically, we will enforce (7), by correcting the estimated departure points $\tilde{\mathbf{x}}_0$ according to $(\tilde{\mathbf{x}}_0)_C = \tilde{\mathbf{x}}_0 + (t - t_0)\nabla\phi$, with $(\tilde{\mathbf{x}}_0)_C$ denoting the corrected departure points. The potential ϕ satisfies the PDE implied by

$$\det\left\{\frac{\partial(\tilde{\mathbf{x}}_0)_C}{\partial\mathbf{x}}\right\} = 1, \quad (8)$$

which happens to be a form of MAE. The latter appears in the fields of mathematical physics [13,25,6,16], differential geometry [49], image registration [33], grid generation [63,10,21], fluid dynamics [11,17,18,22,2], magnetohydrodynamics [71] and cosmology [73]. Seminal work on the MAE goes back to Monge [45], who first posed the problem of optimal mass transport. Questions of existence and uniqueness of solutions to the MAE has been addressed in numerous works, e.g. [43,32,8]. In general the MAE can have more than one solution, and convexity of the solution becomes a necessary condition for uniqueness. In cases where the MAE is solved numerically, convexity can either be enforced through the problem discretization or by the design of the numerical solver [27,4].

The paper is organised as follows: In section 2 we focus on the 2D case of (8) and study the impact of the MA trajectory correction on the anomalous fluid motions that result from numerical approximations. Toward this goal, we use examples of pure rotation and pure deformation to find closed-form solutions to the associated MAEs that help assessing questions of existence and uniqueness of their implied corrections. Section 3 introduces the numerical framework of the MHD flow solver and MA-enhanced trajectory algorithm to be used in the experiments in sections 4 and 5. Section 4 illustrates the effect of the enhanced SL scheme on scalar advection and mass conservation. In section 5 we consider the relaxation of an ideal magnetofluid in 2D and 3D periodic domains, wherein the formation of current sheets leads to changes of the magnetic field’s topology. Section 6 summarizes the main results and concludes the paper.

2 The Monge-Ampère correction

2.1 Preliminaries

A wide class of ODE-like discretizations of the trajectory integral (3) arise as particular cases of the general linear formula (2.4.22) in [31], the two-point subcase of which is particularly relevant to our SL scheme approximation considered here and can be written as

$$\tilde{\mathbf{x}}_0 = \mathbf{x}_i - \Delta t \Phi(t_0, t; \tilde{\mathbf{x}}_0, \mathbf{x}_i) , \quad (9)$$

with $t = t_0 + \Delta t$ and

$$\Phi = c_0 \mathbf{v}(t_0, \tilde{\mathbf{x}}_0) + c \mathbf{v}(t, \mathbf{x}_i) \equiv \tilde{\mathbf{v}} . \quad (10)$$

Here, the weights $c + c_0 = 1$, together with the algorithm used to solve the implicit system of nonlinear equations (9) for the unknowns $\tilde{\mathbf{x}}_0$, determine the form of the discrete integral, whereupon $\tilde{\mathbf{v}}$ is identifiable with a path-mean velocity.

From (4), it can be seen that the vortical part of the velocity does not induce any change in the volume of a fluid element. Consequently, this motivates a correction to the estimated velocities in (10) as the gradient of a scalar potential, so that (9) results in

$$(\tilde{\mathbf{x}}_0)_C = \mathbf{x}_i - \Delta t (\tilde{\mathbf{v}} - \nabla\phi) . \quad (11)$$

Notably, the estimated velocity $\tilde{\mathbf{v}}$ constructed from fields that satisfy the Eulerian form of the mass-continuity equation (5) on the grid does not ensure (6). In particular, the compatibility of (1) and (3) with (6) demands that both Eulerian and Lagrangian forms of the mass continuity equation be fulfilled simultaneously. For an incompressible fluid, this requires that both the prognostic velocity field \mathbf{v} , which is used to construct $\tilde{\mathbf{v}}$, satisfies (5) and that (11) satisfies (8). Therefore, (11) has the interpretation of a path integrated implicit pressure correction to the explicit estimate of $\tilde{\mathbf{v}}$.

Focusing, hereafter, the attention on incompressible flows, the enforcement of the compatibility of (11) with (6) amounts to substituting (11) in (8). This leads readily to a MA equation for the potential ϕ . For simplicity we discuss the 2D case considered in section IV.6.3 of [16]. For any $\Delta t > 0$, the resulting MAE can be written compactly as

$$A\phi_{xx} + 2B\phi_{xy} + C\phi_{yy} + E(\phi_{xx}\phi_{yy} - \phi_{xy}^2) + D = 0 , \quad (12)$$

where subscripts x and y denote the respective partial differentiations. Given

(11), the coefficients of (12) depend only on partial derivatives of $\tilde{\mathbf{v}} = (\tilde{u}, \tilde{v})$, such that

$$\begin{aligned}
A &= 1 - \Delta t \tilde{v}_y \\
B &= 1/2 \Delta t (\tilde{u}_y + \tilde{v}_x) \\
C &= 1 - \Delta t \tilde{u}_x \\
D &= -\tilde{u}_x - \tilde{v}_y - \Delta t (\tilde{u}_y \tilde{v}_x - \tilde{u}_x \tilde{v}_y) \\
E &= \Delta t .
\end{aligned} \tag{13}$$

Solutions to (12) fall into either one of two categories given the discriminant

$$\Lambda \equiv AC - B^2 - DE > 0 , \tag{14}$$

everywhere inside the domain Ω . Solutions of the first type obey the inequalities

$$E\phi_{xx} + C > 0 , \quad E\phi_{yy} + A > 0 ; \tag{15}$$

whereas, those of the second type satisfy

$$E\phi_{xx} + C < 0 , \quad E\phi_{yy} + A < 0 , \tag{16}$$

which are referred to as the type-1 and type-2 solutions, respectively [16]. In particular, the MAE (12) is elliptic if and only if both (14) and (15) are fulfilled, which is necessary to ensure the uniqueness of solutions to (12). Importantly, the Lipschitz condition

$$L \equiv \Delta t \max_i \left(\sum_{j,i} |v^i_{,j}| \right) < 1 , \tag{17}$$

which assures non-intersection of the estimated flow trajectories (9) guarantees (14). Here, the superscript i identifies a component of the velocity vector and the subscript j refers to spatial differentiation [58]. We refer the reader to appendices A and B for further discussion on the existence and unicity of both types of solutions.

2.2 Elemental flows; closed-form solutions.

To develop an intuition for properties of (12) in terms of fluid flow, we examine some of its solutions in the context of the Euler-forward approximation for (9) (i.e. $c_0=0$ and $c = 1$ in (10)) applied to the elemental incompressible pure-rotational $\mathbf{v}_R = \alpha(-y, x)$ and pure-deformational $\mathbf{v}_D = \alpha(y, x)$ flows, where $\alpha = 1s^{-1}$ denotes the flow's amplitude — see fig.1. Accordingly, the tensors of rotation $\Omega_{ik} = 1/2 (\partial u_i / \partial x_k - \partial u_k / \partial x_i)$ and the strain rate $D_{ik} = 1/2 (\partial u_i / \partial x_k + \partial u_k / \partial x_i)$ have the constant entries ($\Omega_{12} = -\Omega_{21} = -\alpha$, $\Omega_{11} = \Omega_{22} = 0$, $\mathbf{D} \equiv 0$) for \mathbf{v}_R and ($D_{12} = D_{21} = \alpha$, $D_{11} = D_{22} = 0$, $\mathbf{\Omega} \equiv 0$) for \mathbf{v}_D .

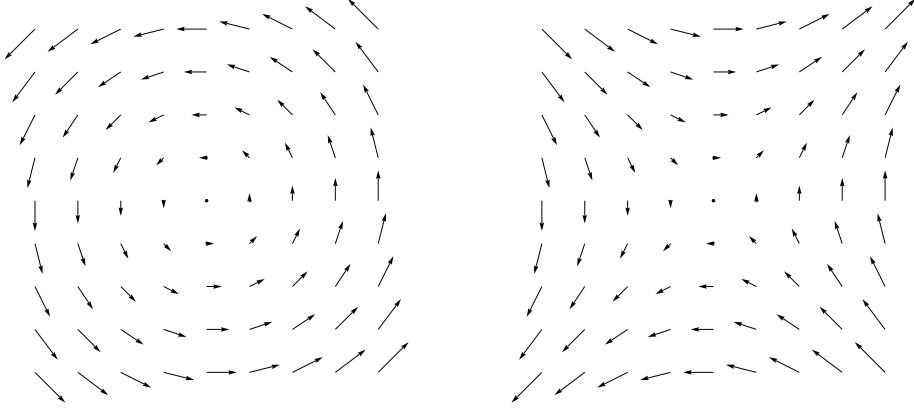


Fig. 1. Examples of incompressible, pure-rotational (left) and pure-deformational flows (\mathbf{v}_R and \mathbf{v}_D).

MAEs associated with \mathbf{v}_R and \mathbf{v}_D are given by, respectively,

$$\phi_{xx} + \phi_{yy} + \Delta t(\phi_{xx}\phi_{yy} - \phi_{xy}^2) + \alpha^2\Delta t = 0 \quad (18)$$

and

$$\phi_{xx} + 2\alpha\Delta t\phi_{xy} + \phi_{yy} + \Delta t(\phi_{xx}\phi_{yy} - \phi_{xy}^2) - \alpha^2\Delta t = 0 . \quad (19)$$

2.2.1 Pure rotation

One can exploit the rotational symmetry of \mathbf{v}_R to find solutions to (18) of the form $\phi(x, y) = F(\xi) \equiv F(x^2 + y^2)$. Substituting F into (18) and using the chain rule yields the second order nonlinear ODE

$$4F_\xi(1 + \Delta tF_\xi) + 4\xi F_{\xi\xi} + 8\Delta t\xi F_\xi F_{\xi\xi} + \alpha^2\Delta t = 0 . \quad (20)$$

Let $G(\xi) = F_\xi$, so that (20) becomes

$$-\frac{4(1 + 2\Delta tG)}{4G(1 + \Delta tG) + \alpha^2\Delta t}dG = \frac{d\xi}{\xi} , \quad (21)$$

which has the general solution

$$G = \frac{-1 \pm (1 - \Delta t^2\alpha^2 - C_s\xi^{-1})^{1/2}}{2\Delta t} , \quad (22)$$

where $C_s > 0$ is an integration constant. Derivatives of F will be real outside the circle $x^2 + y^2 = \xi = C_s/\beta$ centered about the origin, where $\beta = (1 - \alpha^2\Delta t^2)^{1/2}$. Therefore, we let $C_s \rightarrow 0$, which yields the particular solutions

$$F_\pm = -\frac{\xi}{2\Delta t}(1 \mp \beta) + C_\pm , \quad (23)$$

together with the associated trajectory corrections

$$(\tilde{\mathbf{x}}_0)_{C,\pm} = \tilde{\mathbf{x}}_0 + \Delta t F_\xi \nabla \xi = \tilde{\mathbf{x}}_0 - (1 \mp \beta) \mathbf{x}_i . \quad (24)$$

For the purely rotational flow the discriminant (14) becomes

$$\Lambda = 1 - \alpha^2 \Delta t^2 = \beta^2 > 0 ; \quad (25)$$

the type-1 solution satisfies

$$E\phi_{xx} + C = \Delta t \phi_{xx} + 1 > 0, \quad E\phi_{yy} + A = \Delta t \phi_{yy} + 1 > 0 , \quad (26)$$

and the type-2 solution is such that

$$E\phi_{xx} + C = \Delta t \phi_{xx} + 1 < 0, \quad E\phi_{yy} + A = \Delta t \phi_{yy} + 1 < 0 . \quad (27)$$

Indeed, we find

$$F_{xx,\pm} = -\frac{1}{\Delta t} (1 \mp \beta) \quad (28)$$

and therefore one has $F_{xx,+} > -1/\Delta t$ and $F_{xx,-} < -1/\Delta t$. A similar expression yields $F_{yy,+} > -1/\Delta t$ and $F_{yy,-} < -1/\Delta t$. Thus, F_+ and F_- qualify as the type-1 and type-2 solutions, respectively. Observe that for (24) to be well-defined, (25) must be satisfied, for otherwise the correction would have an imaginary part.

The left and right panels of figure 2 illustrate, respectively, the effect of the type-1 and type-2 trajectory corrections implied by (24) for the choice $\alpha \Delta t = 0.85$, which assures (25). Arrival points \mathbf{x}_i (squares), lie on an exact flow trajectory (solid line) and are linked to their respective departure points \mathbf{x}_0 (diamonds) by the thick red lines. Likewise, the \mathbf{x}_i are linked to their corresponding estimated departure points $\tilde{\mathbf{x}}_0$ (circles) by straight line segments that represent the associated estimated trajectories. The set of all estimated departure points (dashed line) and its corresponding set of arrival points therefore may be regarded as the boundaries of initial and final fluid elements, respectively. Black dots show the position of the trajectory correction (11), which amounts to the displacement $\tilde{\mathbf{x}}_0 \rightarrow (\tilde{\mathbf{x}}_0)_C$, everywhere parallel to $\nabla \phi$ (arrows). Notably, the Euler-forward prediction $\mathbf{x}_i \rightarrow \tilde{\mathbf{x}}_0$ deviates away from the exact departure point \mathbf{x}_0 given by (3) and fails to preserve the volume (area in 2D) of the fluid elements. The flow Jacobian associated with the latter is $\hat{J} = 1 + (\alpha \Delta t)^2 > 1$ and indicates that the volume of initial fluid parcels is always larger than that of final elements, which is consistent with the expansion of solid circles into dashed circles seen in fig. 2. The flow Jacobian that corresponds to the forward-in-time motion (i.e. $\tilde{\mathbf{x}}_0 \rightarrow \mathbf{x}_i$), is therefore $J = \hat{J}^{-1} = 1/(1 + (\alpha \Delta t)^2) < 1$ and implies that the trajectory estimates cause final fluid parcels to contract relative to the initial ones. From this perspective — the one that we shall consider in this paper — trajectory errors that

arise from pure rotation are responsible for the anomalous contraction of fluid parcels.

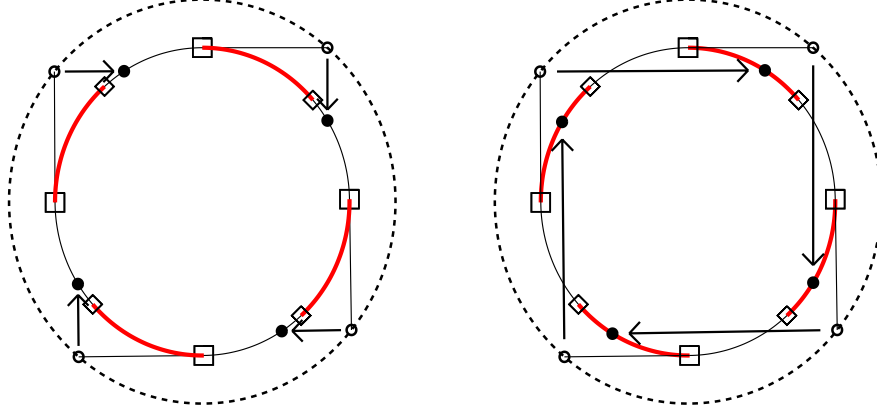


Fig. 2. Anomalous fluid contraction and the type-1 (left) and type-2 (right) MA corrections in the vicinity of the stationary point $(x_o, y_o) = (0, 0)$ for the pure rotational flow. Solid lines denote exact trajectories, whereas; dashed lines mark the set of the departure points. Straight line segments represent computed trajectories that link particular arrival points (squares) to their respective standard departure points (open circles). Arrows indicate the direction of the applied correction that gives the corrected trajectory estimates (black dots).

Observe that the corrected departure points all lie somewhere on the exact flow trajectory for both type-1 and type-2 solutions, so that anomalous contraction is avoided. Also, the corrected departure points lie much closer to the exact solution in the type-1 case than in the type-2 case. Although it is volume-preserving, the type-2 correction lies farther away from the exact solution than the original estimate.

2.2.2 Pure deformation

We now consider solutions to (19), for which no obvious symmetries can be directly determined from the flow geometry, as was the case for \mathbf{v}_R . We will attempt to find exact solutions to (19) by making the assumption that ϕ exists such that $(\tilde{\mathbf{x}}_0)_C \equiv \mathbf{x}_0$, i.e. the trajectory correction yields the exact departure point, which is given by the hyperbolic rotation

$$\begin{pmatrix} x_0 \\ y_0 \end{pmatrix} = \begin{pmatrix} \cosh(\alpha\Delta t) & -\sinh(\alpha\Delta t) \\ -\sinh(\alpha\Delta t) & \cosh(\alpha\Delta t) \end{pmatrix} \begin{pmatrix} x \\ y \end{pmatrix},$$

where $(x, y) = \mathbf{x}_i$ and $(x_0, y_0) = \mathbf{x}_0$. This allows one to construct solutions to (19) from the first order linear PDEs implied by (11)

$$\mathbf{x}_0 - \mathbf{x}_i + \Delta t(\mathbf{v} - \nabla\phi) = 0, \quad (29)$$

from which we find that

$$\phi(x, y) = \left(\frac{x^2 + y^2}{2\Delta t} \right) (\cosh(\alpha\Delta t) - 1) - \frac{xy}{\Delta t} (\sinh(\alpha\Delta t) - \alpha\Delta t) + C, \quad (30)$$

where C is a constant of integration. Substituting (30) into (19) shows that it corresponds to a MAE solution with associated trajectory correction given by

$$\begin{aligned} (\tilde{x}_0)_C &= \tilde{x}_0 + x(\cosh(\alpha\Delta t) - 1) - y(\sinh(\alpha\Delta t) - \alpha\Delta t), \\ (\tilde{y}_0)_C &= \tilde{y}_0 + y(\cosh(\alpha\Delta t) - 1) - x(\sinh(\alpha\Delta t) - \alpha\Delta t). \end{aligned} \quad (31)$$

One can easily verify that (30) satisfies $\phi_{xx}, \phi_{yy} > 0$ for $\alpha\Delta t > 0$ and therefore that it corresponds to a type-1 solution. Effects of (31) for $\alpha\Delta t = 0.7$ and $\alpha\Delta t = 1.7$ are illustrated, respectively, in the left and right panels of figure 3.

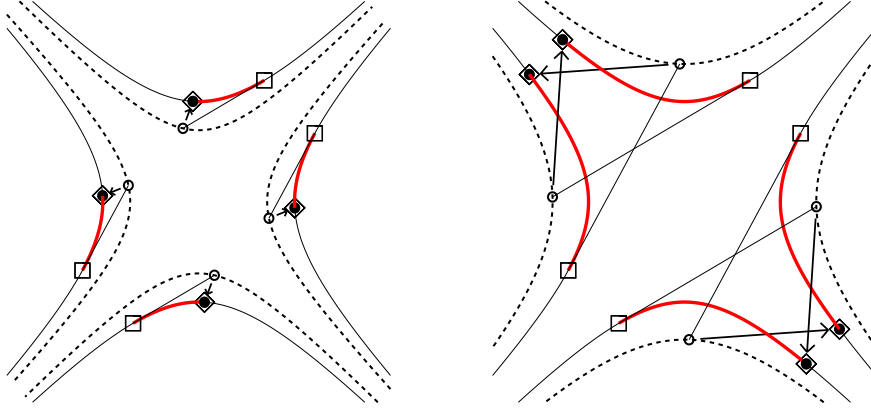


Fig. 3. Anomalous fluid expansion (left) and trajectory intersections (right) with their respective MA correction in the vicinity of the stationary point $(x_o, y_o) = (0, 0)$ for the pure deformational flow.

In this case, the mapping $\tilde{\mathbf{x}}_0 \rightarrow \mathbf{x}_1$ has the Jacobian $J = (1 - (\alpha\Delta t)^2)^{-1}$, which increases monotonically for $0 < \alpha\Delta t < 1$, becomes singular at $\alpha\Delta t = 1$ and is strictly negative for $\alpha\Delta t > 1$. Thus, $\tilde{\mathbf{x}}_0$ is responsible for anomalous expansion when $0 < \alpha\Delta t < 1$ (i.e. $J > 1$ or $0 < \hat{J} < 1$) and trajectory intersections when $\alpha\Delta t > 1$ (i.e. $J < 0, \hat{J} < 0$), as shown by the left and right panels of fig. 3, respectively. Unlike (24), (31) remains well-defined for all timesteps that violate (17), as shown by the case of intersecting flow trajectories depicted here. For instance, the \mathbf{v}_D flow gives $L = 2(1.7) = 3.4 > 1$ for $\alpha\Delta t = 1.7$, thereby violating (17). However, its associated MAE (19) yields $\Lambda = 1 > 0$, so that (14) is satisfied regardless of the value of $\alpha\Delta t$, a special case illustrating that (17) is only sufficient for (14) to be applicable.

A straightforward computation reveals that (29) has no solution when $\mathbf{v} = \mathbf{v}_R$, which implies that solutions to (18) yielding $(\tilde{\mathbf{x}}_0)_C \equiv \mathbf{x}_0$ do not exist.

Furthermore, $\nabla \times (\mathbf{x}_0 - \tilde{\mathbf{x}}_0) = 0$ for the $\mathbf{v} = \mathbf{v}_D$ case, and $\nabla \times (\mathbf{x}_0 - \tilde{\mathbf{x}}_0) \neq 0$ for $\mathbf{v} = \mathbf{v}_R$, meaning that the Helmholtz decomposition of the truncation error for the case of pure rotation has a non-vanishing curl component. Thus, by design, the MA correction is unable to compensate for this part of the trajectory error, which, however, does not produce any change in the parcels' volume — see fig. 2. This property is also what restricts the existence of (24) to cases where (25) is satisfied.

The analysis in terms of the elemental flows shows that anomalous fluid contraction and expansion due to Euler-forward trajectory approximations can be attributed to, respectively, pure rotation and pure deformation. In particular, the case of pure deformation shows that the physical realizability of the flow can be compromised by trajectory intersections arising from the anomalous motions if (8) is not ensured. The example of pure rotation has shown that either type-1 or type-2 solutions were possible candidates for a trajectory correction. The type-2 trajectory correction provided a less accurate (although volume-preserving) estimate than the prediction given by the Euler-forward scheme, whereas; the type-1 correction was both more accurate and volume-preserving.

In general the shear $\nabla \mathbf{u} = \mathbf{\Omega} + \mathbf{D}$ is a combination of rotation and deformation. Thus, although elemental flows provide insight into the mechanics of the MAE enhancement of the standard SL scheme, assessing the impact of (11) on the physics of fluids requires the use of a numerical solver.

3 Numerical implementation

3.1 MHD solver

To assess the impact of the MA trajectory correction onto the flow solution we consider the physical system studied in [1], which consists of the perfectly conducting, constant density magneto-fluid described by the classical MHD incompressible Navier-Stokes equations

$$\frac{d\mathbf{v}}{dt} = -\nabla\pi' + \frac{1}{\rho_o\mu_o}\mathbf{B} \cdot \nabla\mathbf{B} + \nu\nabla^2\mathbf{v} , \quad (32)$$

$$\frac{d\mathbf{B}}{dt} = \mathbf{B} \cdot \nabla\mathbf{v} , \quad (33)$$

$$\nabla \cdot \rho_o\mathbf{v} = 0 , \quad (34)$$

$$\nabla \cdot \mathbf{B} = 0 , \quad (35)$$

where \mathbf{B} is the magnetic field vector (in Tesla units) and π' incorporates both a density-normalised pressure perturbation and magnetic pressure [56]. Here we use $\rho_o = 1\text{kg m}^{-3}$ and $\mu_o = 1\text{N A}^{-2}$, with $\nu = 0.0039\text{m}^2\text{s}^{-1}$ denoting a uniform, constant kinematic viscosity.

Using (35), the Lorentz force $\mathbf{B} \cdot \nabla \mathbf{B}$ and magnetic induction $\mathbf{B} \cdot \nabla \mathbf{v}$ terms are further written in conservative form

$$\mathbf{B} \cdot \nabla B^I = \nabla \cdot (\mathbf{B} B^I), \quad \mathbf{B} \cdot \nabla v^I = \nabla \cdot (\mathbf{B} v^I), \quad (36)$$

where I stands for the I^{th} components of (32) and (33).

To outline numerical approximations for the system (32)-(35) it is useful to symbolize the prognostic equations of the system in the form of (1)

$$\frac{d\boldsymbol{\Psi}}{dt} = \mathbf{R}, \quad (37)$$

where $\boldsymbol{\Psi} = \{\mathbf{v}, \mathbf{B}\}^T$ and $\mathbf{R} = \{\mathbf{R}_v, \mathbf{R}_B\}^T$ denote, respectively, the vectors of prognosed dependent variables and associated forcings on the rhs of (32) and (33).

The equations (37) are integrated using the MHD extension of the EULAG model, a general-purpose simulation code built on the non-oscillatory forward-in-time algorithms — see [56] for a detailed exposition —

$$\boldsymbol{\Psi}_i^n = LE_i(\widetilde{\boldsymbol{\Psi}}) + 0.5\Delta t \mathbf{R}_i^n \equiv \widehat{\boldsymbol{\Psi}}_i + 0.5\Delta t \mathbf{R}_i^n, \quad (38)$$

where $\boldsymbol{\Psi}_i^n$ is the solution sought at the grid point (t^n, \mathbf{x}_i) , $\widetilde{\boldsymbol{\Psi}} \equiv \boldsymbol{\Psi}^{n-1} + 0.5\Delta t \mathbf{R}^{n-1}$, and LE denotes a two-time-level, optionally advective semi-Lagrangian [58] or flux-form Eulerian [57] nonoscillatory transport operator (viz. advection scheme). Because of the focus of the current paper on the semi-Lagrangian integrations of the governing equations such as (32)-(35), the template algorithm (38) is thought as a realization of the trapezoidal approximation of the path integral (1).

To allow for such features as grid adaptivity and to facilitate the implementation of boundary conditions in the possibly time-dependent geometries (e.g. spherical, cylindrical, etc.) that some problems dictate, EULAG performs all computations (38) in a computational space $(\bar{t}, \bar{\mathbf{x}})$, distinct, in general, from the physical space (t, \mathbf{x}) , in which the solution is sought [51]. Here we shall restrict ourselves to the impact of the MA correction in the context of static and uniform Cartesian meshes, in which case both spaces are identical $(\bar{t}, \bar{\mathbf{x}}) \equiv (t, \mathbf{x})$.

The template algorithm (38) is implicit with respect to all prognosed dependent variables and must be inverted algebraically subject to the discrete forms

of the divergence constrains (34) and (35). To achieve this, (38) is written as a fixed-point iteration

$$\Psi_{\mathbf{i}}^{n,\nu} = \widehat{\Psi}_{\mathbf{i}} + 0.5\Delta t \mathbf{L}(\Psi)_{\mathbf{i}}^{n,\nu} + 0.5\Delta t \mathbf{N}(\Psi)_{\mathbf{i}}^{n,\nu-1} - 0.5\Delta t \nabla \Phi|_{\mathbf{i}}^{n,\nu}, \quad (39)$$

that separates \mathbf{R} into terms that are linear $\mathbf{L}(\Psi)$ and nonlinear $\mathbf{N}(\Psi)$ with respect to Ψ as well as a gradient of the potential $\Phi = (\pi', \pi', \pi', \pi^*, \pi^*, \pi^*)$ that incorporates the physical pressure gradient of (32) together with $\nabla \pi^*$, an auxiliary perturbation added to the rhs of (33) that compensates truncation error departures from (35) at each outer iteration ν of (39). Lagging the non-linear term behind all the other terms in (39) enables one to recover a closed form expression for $\Psi_{\mathbf{i}}^{n,\nu}$ linear in $\Phi_{\mathbf{i}}^{n,\nu}$

$$\Psi_{\mathbf{i}}^{n,\nu} = [\mathbf{I} - 0.5\Delta t \mathbf{L}]_{\mathbf{i}}^{-1} \left(\widehat{\Psi} - 0.5\Delta t \nabla \Phi^{n,\nu} \right), \quad (40)$$

where $\widehat{\Psi} = \widehat{\Psi} + 0.5\Delta t \mathbf{N}(\Psi)^{n,\nu-1}$. Acting on (40) with the discrete analogs of (34) and (35) produces two large sparse linear, generally nonsymmetric systems which are then inverted for π' and π^* by using the preconditioned generalized conjugate residual (GCR) method [23], highlighted in the next section. The trapezoidal integral in (39) assumes that all contributions to \mathbf{R} are treated to second-order accuracy. However, here we treat the Fickian diffusion term on the rhs of (32), which we denote by $\widetilde{\mathbf{R}}$, separately from other forcings by reproducing the Euler forward integral structure in the argument of the transport operator LE in (38): $\widetilde{\Psi} \equiv \Psi^{n-1} + 0.5\Delta t (\mathbf{R} + 2\widetilde{\mathbf{R}})$. Upon recovery of $\Psi^{n,\nu}$, the total implicit forcing $\mathbf{R}\mathbf{I} = \mathbf{L}\Psi - \nabla \Phi$ is returned as $\mathbf{R}\mathbf{I}^n = (0.5\Delta t)^{-1}(\Psi^{n,\nu} - \widehat{\Psi})$; whereas, the total explicit forcing $\mathbf{R}\mathbf{E}^n = \mathbf{N}(\Psi) + \widetilde{\mathbf{R}}$ is obtained from its definition using the updated solution $\Psi^{n,\nu}$.

In the actual implementation, the sequence of steps that leads from $\Psi^{n,\nu-1}$ to $\Psi^{n,\nu}$ consists of two consecutive blocks that amount to, respectively, the solution of (32)-(34) and (33)-(35). Each step in the sequence $\nu = \{1, \dots, \nu^*\}$ uses the most current update of the velocity and magnetic field, whenever those are made available inside each block. The first block begins with finding a first guess for the magnetic field through the inversion of the evolutionary form of (33)

$$\mathbf{B}_{\mathbf{i}}^{\nu-1/2} = \widehat{\mathbf{B}}_{\mathbf{i}} + 0.5\Delta t (\mathbf{B}^{\nu-1/2} \cdot \nabla \mathbf{v}^{\nu-1})_{\mathbf{i}}, \quad (41)$$

in which an $\mathcal{O}(\Delta t^2)$ estimate of the velocity $\mathbf{v}^0 = 2\mathbf{v}^{n-1} - \mathbf{v}^{n-2}$ is used at $\nu = 1$. Here the superscript $\nu - 1/2$ means that (41) is half-way from the completion of the outer iteration. Together, $\widehat{\mathbf{v}}_{\mathbf{i}}$ and (41) produce the explicit part of (40), which now becomes available for the solution of the elliptic problem for π'

$$\mathbf{v}_{\mathbf{i}}^{\nu} = \widehat{\mathbf{v}}_{\mathbf{i}} + \frac{0.5\Delta t}{\rho_o \mu_o} (\nabla \cdot \mathbf{B}\mathbf{B})_{\mathbf{i}}^{\nu-1/2} - 0.5\Delta t \nabla \pi'|_{\mathbf{i}}^{\nu}$$

$$\frac{1}{\rho_o}(\nabla \cdot \rho_o \mathbf{v})_{\mathbf{i}}^{\nu} = 0 . \quad (42)$$

The second block begins with finding a new solution to (41) using the updated velocity

$$\mathbf{B}_{\mathbf{i}}^{\nu-1/4} = \widehat{\mathbf{B}}_{\mathbf{i}} + 0.5\Delta t(\mathbf{B}^{\nu-1/4} \cdot \nabla \mathbf{v}^{\nu})_{\mathbf{i}} , \quad (43)$$

to be used in the elliptic problem for π^*

$$\begin{aligned} \mathbf{B}_{\mathbf{i}}^{\nu} &= \widehat{\mathbf{B}}_{\mathbf{i}} + 0.5\Delta t(\nabla \cdot \mathbf{B}^{\nu-1/4} \mathbf{v}^{\nu})_{\mathbf{i}} - 0.5\Delta t \nabla \pi^*|_{\mathbf{i}}^{\nu} \\ (\nabla \cdot \mathbf{B})_{\mathbf{i}}^{\nu} &= 0 , \end{aligned} \quad (44)$$

the solution of which completes the outer iteration. Typically, two or three iterations are sufficient for a practically converged solution, and so here we use $\nu^* = 2$ [56].

3.2 Trajectory schemes

We approximate path integrals (3) by selecting either of $c_0 = 0$ and $c_1 = 1$ or $c_0 = c_1 = 1/2$ in (10). The former gives the Euler-forward approximation to (3)

$$\mathbf{x}_0^0 \equiv \mathbf{x}_{\mathbf{i}} - \Delta t \mathbf{v}(\mathbf{x}_{\mathbf{i}}, t) \quad (45)$$

that either provides the final approximation or the initial iterate for the second-order-accurate mid-point rule

$$\mathbf{x}_0^{\kappa} = \mathbf{x}_{\mathbf{i}} - \frac{1}{2}\Delta t(\mathbf{v}(\mathbf{x}_0^{\kappa-1}, t_0) + \mathbf{v}(\mathbf{x}_{\mathbf{i}}, t)) \quad , \quad \kappa = 1, \dots, \kappa^* , \quad (46)$$

that arises from the latter choice of coefficients. Two iterations of (46) suffice for a second-order accuracy, while its convergence is assured provided the Lipschitz constant L (17) is smaller than unity [58]. First-order linear extrapolation of $\mathbf{v}(\mathbf{x}_{\mathbf{i}}, t_0)$ gives an estimate of $\mathbf{v}(\mathbf{x}_{\mathbf{i}}, t)$ and a fourth-order-accurate monotone interpolation procedure is used to map the former to the footpoint of the estimated trajectory $\mathbf{v}(\mathbf{x}_{\mathbf{i}}, t_0) \rightarrow \mathbf{v}(\mathbf{x}_0^{\kappa-1}, t_0)$ [59].

Once the estimated departure points are obtained from (45) or (46), they are corrected according to (11);

$$(\tilde{\mathbf{x}}_0)_{\mathbf{C}} = \tilde{\mathbf{x}}_0^{\kappa^*} + \Delta t \nabla \phi , \quad \kappa^* = 0, 1, 2, \dots . \quad (47)$$

To obtain ϕ , we solve approximately the nonlinear boundary value problem given by substitution of (47) into (8)

$$\mathcal{F}(\phi)_{\mathbf{i}} \equiv \det \left\{ \frac{\partial (\tilde{\mathbf{x}}_0)_{\mathbf{C}}}{\partial \mathbf{x}} \right\}_{\mathbf{i}} - 1 = 0 , \quad (48)$$

where $\partial/\partial\mathbf{x}$ symbolizes centered finite-differences. For simplicity, we employ periodic boundary conditions for the trajectory correction, $\nabla\phi$, in (11) and use a Jacobian-Free Newton-Krylov (JFNK) approach to find a solution to (48) [40,37,71]. Under condition (17), periodicity implies that the only admissible solutions are type-1 — see the discussion in appendices A and B.

JFNK methods derive from the expansion of (48) into a multivariate Taylor series

$$\mathcal{F}_i(\phi^{m+1}) = \mathcal{F}_i(\phi^m) + (\mathcal{J}(\phi^m)\delta\phi^m)_i + \text{H.O.T.} \quad (49)$$

where $\mathcal{J} = \partial\mathcal{F}/\partial\phi$ is the $N \times N$ Jacobi matrix of \mathcal{F} with N representing the number of grid points, $\delta\phi^m = \phi^{m+1} - \phi^m$ and H.O.T. denote the higher-order terms of the expansion. Neglecting H.O.T. and setting $\mathcal{F}_i(\phi^{m+1}) = 0$ gives rise to the classical Newton's method: for any initial guess ϕ^0 ,

For $m = 0, 1, 2, \dots$ until convergence do :

$$\text{Solve } (\mathcal{J}(\phi^m)\delta\phi^m)_i + \mathcal{F}_i(\phi^m) = 0 \quad \text{for } \delta\phi_i^m, \quad (50)$$

$$\text{Set } \phi_i^{m+1} = \phi_i^m + \delta\phi_i^m, \quad (51)$$

$$\text{Exit if } \|r^{m+1}\|/\|r^0\| \leq \varepsilon, \quad (52)$$

enddo.

where $\|\cdot\|$ is a user-defined norm, $r^m = \mathcal{F}(\phi^m)$ is the residual and $\varepsilon < 1$. Using a direct method to solve (50) requires explicit evaluation and storage of \mathcal{J} 's entries. However, in problems arising from physical applications, obtaining an analytical expression for \mathcal{J} may not always be practical or possible. In particular, the cost of storing matrix entries when the number of unknowns is large ($N \approx 10^6 - 10^7$ in this study) may become prohibitively expensive memory-wise. Instead, we solve (50) approximately using an iterative Krylov method until the following convergence criterion is satisfied

$$\|\mathcal{J}(\phi^m)\delta\phi^m + \mathcal{F}(\phi^m)\| \leq \eta_m \|\mathcal{F}(\phi^m)\|, \quad (53)$$

where η_m is the so-called forcing term, which controls the accuracy of the linearized problem (50) [9]. The forcing term must be chosen such as to avoid solving (50) with unnecessary accuracy (viz. oversolving) and to assure quadratic convergence of the Newton iteration when sufficiently close to the solution. This is done using the approach discussed in section 6.3 of [35], in which

$$\eta_m = \min(\eta_{\max}, \max(\eta_m^C, 0.5\tau_t/\|\mathcal{F}(\phi^m)\|)) , \quad (54)$$

$$\eta_m^C = \begin{cases} \eta_{\max}, & m = 0 \\ \min(\eta_{\max}, \eta_m^A), & m > 0, \gamma\eta_{m-1}^2 \leq 0.1 \\ \min(\eta_{\max}, \max(\eta_m^A, \gamma\eta_{m-1}^2)), & m > 0, \gamma\eta_{m-1}^2 > 0.1 \end{cases} \quad (55)$$

and $\eta_m^A = \gamma(\|\mathcal{F}(\phi^m)\|/\|\mathcal{F}(\phi^{m-1})\|)^2$ and $\tau_t = \tau_a + \tau_r\|\mathcal{F}(\phi^0)\|$. In contrast to [35], where $\|\cdot\|$ denotes the Euclidean norm in \mathbb{R}^N (e.g. L^2), here it represents

the L_∞ norm.

To reduce the effort in coding and because of our own experience with the numerical machinery already imbedded in the EULAG-MHD model, we seek the solution of (50) by employing the GCR algorithm, the use of which is first and foremost intended for the solution of elliptic problems (42) and (44). For the reader's convenience, here we outline GCR as customized for (50). Toward this end, we write the linear system (50) as

$$\mathcal{L}(\delta\phi^m) = \mathcal{Q} , \quad (56)$$

where $\mathcal{L}(\delta\phi^m) \equiv \mathcal{J}(\phi^m)\delta\phi^m$ and $\mathcal{Q} \equiv -\mathcal{F}(\phi^m)$. As a result of its use in all-scale atmospheric applications on the sphere, the formulation of the GCR solver in EULAG-MHD allows for operator preconditioning. Left-preconditioning is assumed, which consists in replacing (56) with the alternate problem

$$\mathcal{P}^{-1}[\mathcal{L}(\delta\phi^m) - \mathcal{Q}] = 0 , \quad (57)$$

where \mathcal{P} is the preconditioning operator. Under this assumption, augmenting (56) with a k th-order damped oscillation equation and using variational arguments that determine the parameters of its discretization to assure the minimization of the residual errors $\langle aa \rangle$ in the norm defined by the inner product $\langle \cdot \cdot \rangle$ leads to the following algorithm for the progression of the solution [65]. For any initial guess $\delta\phi^{m,0}$, set $a_{\mathbf{i}}^0 = \mathcal{L}(\delta\phi^{m,0}) - \mathcal{Q}_{\mathbf{i}}$, $p_{\mathbf{i}}^0 = \mathcal{P}_{\mathbf{i}}^{-1}(a^0)$; then iterate:

$$\begin{aligned} & \text{For } i = 1, 2, \dots \text{ until convergence do} \\ & \quad \text{for } j = 0, \dots, k-1 \text{ do} \\ & \quad \quad \beta = -\frac{\langle a^j \mathcal{L}(p^j) \rangle}{\langle \mathcal{L}(p^j) \mathcal{L}(p^j) \rangle} , \\ & \quad \quad \delta\phi_{\mathbf{i}}^{m,j+1} = \delta\phi_{\mathbf{i}}^{m,j} + \beta p_{\mathbf{i}}^j , \\ & \quad \quad a_{\mathbf{i}}^{j+1} = a_{\mathbf{i}}^j + \beta \mathcal{L}_{\mathbf{i}}(p^j) , \\ & \quad \quad \text{exit if } \|a^{j+1}\| \leq \eta_m \|r^m\| , \\ & \quad \quad q_{\mathbf{i}} = \mathcal{P}_{\mathbf{i}}^{-1}(a^{j+1}) , \\ & \quad \quad \text{Evaluate } \mathcal{L}_{\mathbf{i}}(q) , \\ & \quad \quad \forall_{l=0,j} \alpha_l = \frac{\langle \mathcal{L}(q) \mathcal{L}(p^l) \rangle}{\langle \mathcal{L}(p^l) \mathcal{L}(p^l) \rangle} , \\ & \quad \quad p_{\mathbf{i}}^{j+1} = a_{\mathbf{i}}^{j+1} + \sum_{l=0}^j \alpha_l p_{\mathbf{i}}^l , \\ & \quad \quad \mathcal{L}_{\mathbf{i}}(p^{j+1}) = \mathcal{L}_{\mathbf{i}}(a^{j+1}) + \sum_{l=0}^j \alpha_l \mathcal{L}_{\mathbf{i}}(p^l) , \\ & \quad \quad \text{end do} , \\ & \quad \text{reset } [\delta\phi^m, a, p, \mathcal{L}(p)]_{\mathbf{i}}^k \text{ to } [\delta\phi^m, a, p, \mathcal{L}(p)]_{\mathbf{i}}^0 , \\ & \quad \text{end do} . \end{aligned}$$

Only one matrix-vector operation per solver iteration is needed in the above procedure, which we approximate as

$$\mathcal{L}_i(q) = (\mathcal{J}(\phi^m)q)_i \approx \frac{\mathcal{F}_i(\phi^m + \epsilon(\phi^m, q)q) - \mathcal{F}_i(\phi^m)}{\epsilon(\phi^m, q)}, \quad (58)$$

whereupon no knowledge of the Jacobi matrix itself is needed, hence the name ‘Jacobian-Free’. To ensure that ϕ^m is properly perturbed each time (58) is evaluated, the increment ϵ is scaled according to

$$\epsilon(\phi, q) := \max(|\langle \phi^m q \rangle| / \|q\|_2, 1.) \operatorname{sgn}(\langle \phi^m q \rangle) h / \|q\|_2, \quad (59)$$

where $\|\cdot\|_2$ symbolizes the L^2 norm; see [9] for a detailed discussion on the definition of (59). Since (58) is $\mathcal{O}(\epsilon)$ -accurate, h must be larger than the machine epsilon ϵ_{mach} to prevent contamination by cancellation errors. In our double-precise calculations we have used $h = \mathcal{O}(\sqrt{\epsilon_{\text{mach}}}) = 1 \times 10^{-7}$ [35]. Our solver uses $\delta\phi^{m,0} = 0$, initializes ϕ^0 with the solution from the previous timestep and employs parameters $k = 2$, $\gamma = 0.9$, $\eta_{\text{max}} = 0.5$, $\tau_a = 1 \times 10^{-15}$ and $\tau_r = 1 \times 10^{-7}$ for the absolute and relative error tolerances, respectively.

The GCR solver used for the solution of elliptic problems (42) and (44) employs a line-relaxation preconditioner based on an implicit Richardson iteration [65]. Although one could devise a similar approach for (48) and incorporate it into the JFNK framework, here we do not study the impact of left-preconditioning on the convergence of the solution and chose $\mathcal{P} = \mathcal{I} \equiv$ the identity matrix.

Mappings of $\tilde{\Psi}$ variables to the departure points given by either of (45), (46) or (47) are carried out with the fourth-order-accurate monotone interpolation scheme and give the output of the LE operator in (38).

4 Scalar advection

Scalar advection experiments were first used in [15] to demonstrate the benefit of the MA trajectory correction for mass and shape preservation. In this section we use similar experiments to analyze the impact of the solver’s accuracy and to present a concrete example of anomalous fluid contraction produced by standard trajectory estimates (cf. section 2.2.1). Solutions are sought for two different initial scalars using a cellular flow given by the stream-function $\zeta = \sin(x)\sin(y)$, with $(x, y) \in [-\pi, \pi] \times [-\pi, \pi]$. The first scalar is specified as $\psi_1 = \max(0, 2|\zeta - 7|)$; sine hills located at the center the flow’s vortices, whereas; the second uses the same distribution shifted to the right by $\delta x = 0.25\pi$ (hereafter, ψ_2). Each panel of figure 4 shows isolines of initial/evolved scalars in a single cell $[0, \pi] \times [0, \pi]$ at a time $t^* = t/\tau$, where

t is physical time and $\tau \equiv \pi/1 \text{ ms}^{-1} \approx 3.14s$ is defined as the cell's turn-over time. The latter is displayed at the top of each figure, along with the

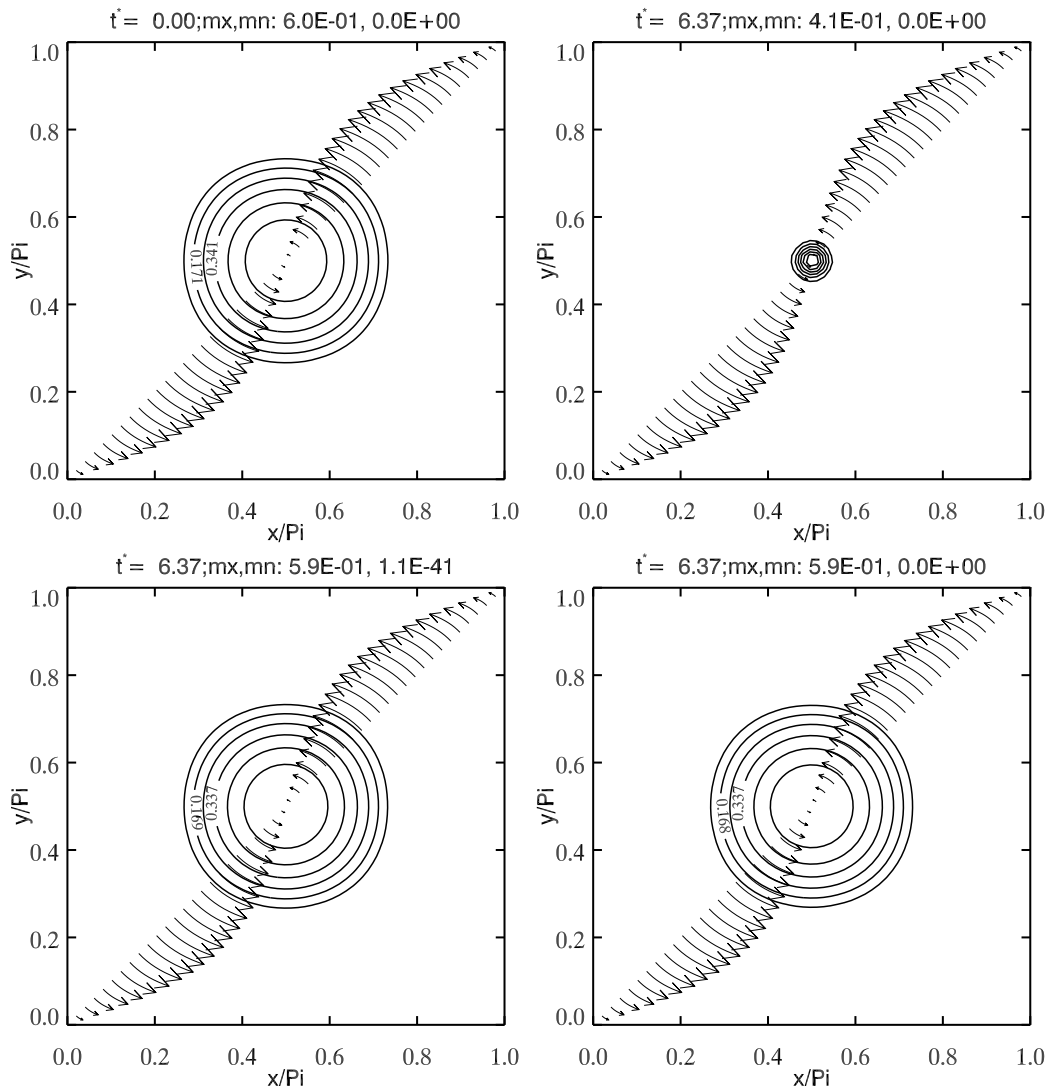


Fig. 4. Initial and evolved passive scalars for selected runs displayed in table 1. Each panel shows a snapshot of a tracer's isolines, where arrows denote the magnitude of the constant flow velocity along a panel's diagonal. The time at which each snapshot is taken, along with the minimum and maximum of the advected scalar are displayed at the top of each panel. The upper left panel shows the initial condition for the ψ_1 -experiments. Classical SL (run 1-1-0) and MA-enhanced results (run 1-1-2) are plotted, respectively, after 6.4 turn-over times in the top-right and bottom-left panels. The bottom-right panel shows the solution of run 1-2-0 at the same instant.

minimum (mn) and maximum (mx) of the advected scalar. Arrows mark flow trajectories and indicate the flow magnitude and direction across the domain. Table 1 shows statistics of scalar advection experiments using either of ψ_1 or ψ_2 as initial condition. Each row displays, from left to right, the identifier of the experiment, the L_∞ norm of the MA solver residual, its variance σ , the

SL run	$ \hat{J} - 1 _\infty$	σ	t^*	$\delta\psi(t)$	$\delta\psi^2(t)$
1-1-0	4.00×10^{-2}	4.00×10^{-2}	6.38	-0.9759	-0.9813
1-1-2	1.37×10^{-4}	9.20×10^{-5}	6.38	-0.0021	-0.0105
1-1-4	1.98×10^{-6}	1.98×10^{-6}	6.38	0.0062	-0.0010
1-2-0	4.03×10^{-4}	3.95×10^{-4}	6.38	-0.0214	-0.0320
1-2-2	1.37×10^{-7}	1.37×10^{-7}	6.38	0.0053	-0.0009
1-2-0	4.03×10^{-3}	3.95×10^{-4}	315.29	-0.8101	-0.8728
1-2-2	1.37×10^{-7}	1.37×10^{-7}	315.29	0.1014	0.0347
2-1-0	4.00×10^{-2}	4.00×10^{-2}	6.38	-0.9087	-0.9685
2-1-2	1.37×10^{-4}	9.20×10^{-5}	6.38	-0.0372	-0.2327

Table 1

Results of scalar advection experiments. The first integer in the first column indicates which initial condition is used (i.e. ψ_1 or ψ_2), the second stands for the order of accuracy of the trajectory scheme and the third is the base-10 logarithm of ε (zero means no correction is performed). The second and third columns show, respectively, the L_∞ norm and variance of the inverse flow Jacobian residual. The fourth column displays the non-dimensional time corresponding to the first and second moments of the conservation error, which are shown in the fifth and sixth columns, respectively.

time t^* at which the data has been taken, and finally the first and second moments of the conservation error $\delta\psi \equiv \int_\Omega \psi(t) dV / \int_\Omega \psi(t=0) dV - 1$ and $\delta\psi^2 \equiv \int_\Omega \psi(t)^2 dV / \int_\Omega \psi(t=0)^2 dV - 1$. The first slot in the identifier of each experiment corresponds to the initial condition used (i.e. $i = \{1, 2\}$ for ψ_i), next comes the order of accuracy of the trajectory scheme that is employed (i.e. first-order or second-order) and finally the logarithm to the base 10 of the convergence threshold ε , with zero meaning that no correction has been applied.

Isolines of ψ_1 , shown as solid lines in the top-left panel of fig. 4, are, to a constant, identical to the streamlines and therefore $\mathbf{v} \cdot \nabla\psi_1 = 0$ implies that $\partial\psi_1/\partial t = 0$. Top-right and bottom-left panels show, respectively, the evolved ψ_1 scalar distribution resulting from the uncorrected scheme (run 1-1-0) and the solution obtained by applying the MA trajectory correction using $\varepsilon = 1 \times 10^{-2}$ (run 1-1-2) at $t^* = 6.38$. Scalar isolines, also identifiable with boundaries of fluid elements, have moved inwards toward the center of the vortex in the solution using the uncorrected scheme as a result of the anomalous fluid contraction, whereas; those of the MA-enhanced solution appear almost unchanged by the revolutions — see figure 2 for an illustration of anomalous fluid contraction produced by first-order-accurate trajectory estimates. While

the former has lost more than 98% of its total mass and 33% of its amplitude after ≈ 6 revolutions, the latter only suffered 0.2% mass and 2% amplitude losses — see table 1. Imposing $\varepsilon = 1 \times 10^{-4}$ (run 1-1-4) instead produces a 0.6% mass increase and improves the conservation of $\delta\psi^2$ by a factor of 10 with respect to run 1-1-2. The solution of run 1-2-0 (bottom right panel), which uses second-order-accurate uncorrected trajectory estimates, can hardly be distinguished from the MA-enhanced solution of run 1-1-2 by its isolines, apart from a 10 times larger mass loss.

The top-left panel of fig. 5 shows the tracer that results from corrected second-order-accurate trajectory estimates (run 1-2-2). Its solution is qualitatively

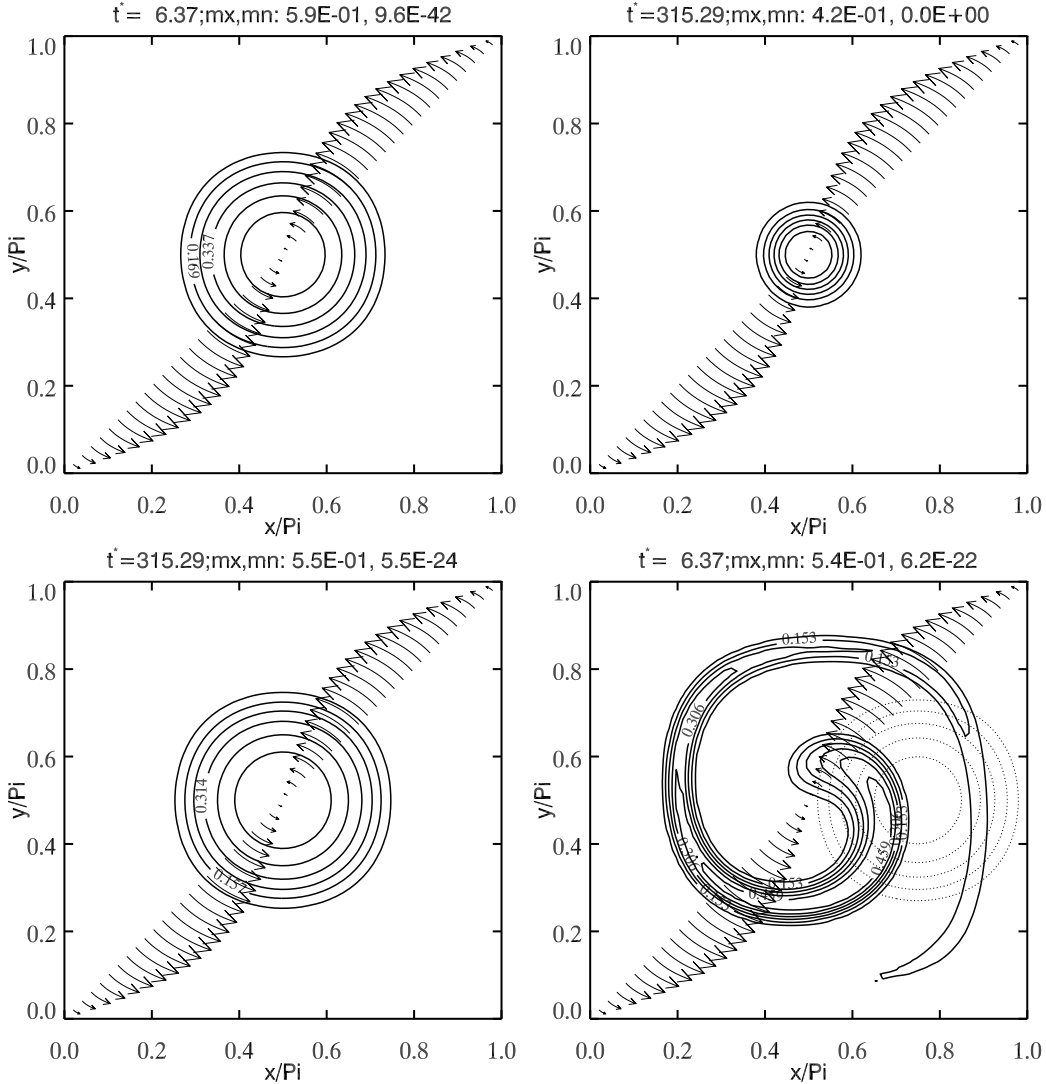


Fig. 5. Evolved passive scalars for run 1-2-2 at $t^* = 6.38$ (top left), run 1-2-0 at $t^* = 315.29$ (top right), run 1-2-2 at $t^* = 315.29$ (bottom left) and run 2-1-2 at $t^* = 6.38$, which uses ψ_2 (pale dotted lines) as initial condition (bottom right).

similar to those of runs 1-1-2 and 1-2-0, as far as its shape is concerned.

SL run	$\min\{\Lambda\}$	$\min\{E\phi_{xx} + C\}$	$\min\{E\phi_{yy} + A\}$
1-1-2	0.9200	0.5934	0.5935
1-1-4	0.9200	0.5934	0.5935
1-2-2	0.1939	0.8168	0.8168

Table 2

Properties of MAE solutions found for scalar advection tests. The first column displays the run’s identifier, the second displays the minimum on the grid of the discriminant Λ in (14), and the last two columns show the minima of functions $E\phi_{xx} + C$ and $E\phi_{yy} + A$ that are used to discriminate between type-1 and type-2 solutions, as per inequalities (15) and (16).

However, it loses 4 times less mass than run 1-2-0 and has a $\delta\psi^2$ smaller by two orders of magnitude. Notably, runs 1-2-2 and 1-1-4 give basically the same statistics. Top right and bottom left panels show, respectively, the solutions of runs 1-2-0 and 1-2-2 after ≈ 315 turn-over times, at which point the MA-enhanced solution still gives a result that looks very similar to the tracer obtained after only six turn-over times, whereas; the classical SL solution exhibits noticeable anomalous contraction of the fluid elements. Thus, even when employing a second-order-accurate trajectory scheme, the standard SL solution loses 81% of its total mass after a very long time; whereas, the MA-enhanced run gains a mere 10%.

The bottom-right panel of figure 5 shows the result of MA-enhanced advection for the ψ_2 scalar (run 2-1-2), where the initial scalar is represented by the pale dotted lines. Unlike ψ_1 , ψ_2 does not satisfy $\mathbf{v} \cdot \nabla\psi_2 = 0$ at $t^* = 0$ and transport occurs perpendicular to the isolines, thereby leading to the formation of filamentary structures that prevent an equally accurate treatment by the interpolation algorithm. Consequently, the MA-enhanced run loses ≈ 15 times more mass when evolving ψ_2 than ψ_1 (run 1-1-2). Nevertheless, this loss is still only 4%, as opposed to 91% for the uncorrected scheme (run 2-1-0). Thus, even though runs 1-1-2 and 2-1-2 both use the same set of corrected departure points, the accuracies to which they effectively enforce (6) differs entirely as a result of interpolation.

The analysis of the 2D MAEs in section 2 shows that type-1 and type-2 solutions are the only possible candidates for a trajectory correction if (14) is satisfied. Moreover, the type-1 solution turned out to be the most accurate for the case of pure rotation. The discussion in appendix B further shows that type-2 solutions are forbidden by periodic boundary conditions if (17) is satisfied. Table 2 displays the properties of MAE solutions that were found in the context of scalar advection tests, for which $L \approx 0.4 < 1$. The first column shows the identifier of each MA-enhanced run, the second shows the minimum of the discriminant Λ in (14); whereas, third and fourth columns show

the minima of functions $E\phi_{xx} + C$ and $E\phi_{yy} + A$ that are used to discriminate between type-1 and type-2 solutions based on (15) and (16), respectively. Since (14) and (15) are fulfilled by all three solutions, they are all type-1, which is in accordance with the theoretical predictions.

Scalar advection tests demonstrate that the MA-enhanced solutions supersede those of the standard SL scheme with respect to the accuracy to which (6) is enforced. The impact of the MA enhancement of the estimated departure points on conservativity, however, is ultimately controlled by interpolation, which becomes a key player in the numerical realization of (6) whenever sharp gradients appear in the solution — recall the discussion in the introduction.

5 Relaxation of an ideal magneto-fluid

The zero-resistivity plasma described by equations (32)-(35) belongs to ideal MHD, a special case of the general MHD approximation. In this regime, the magnetic flux through a material fluid surface is constant and the field lines are said to be ‘frozen’ into the fluid, as per Alfvén’s theorem [26]. Consider the situation where fluid motions have brought into contact two surfaces having zero normal magnetic flux, or simply flux surfaces. If the tangential component of \mathbf{B} at their common interface changes direction discontinuously as one moves across it, we say that a tangential discontinuity (TD) has formed. By Ampère’s law ($\nabla \times \mathbf{B} = \mu_0 \mathbf{j}$), a TD implies the existence of a thin layer of increased current density \mathbf{j} , or current sheet (CS) [47]. For this reason, the terms TD and CS refer to the same physical entity and they may be used interchangeably. In a real plasma with finite but small resistivity, the enhanced dissipation of magnetic energy (ME) within the CS can lead to a local breakdown of the frozen-in condition thereby allowing field lines pertaining to each flux surface to reconnect [1]. Consequently, reconnection is accompanied by a release of ME into other forms of energy, such as kinetic and internal energies. It is fundamental to explaining phenomena such as solar coronal mass ejections, flares, and geomagnetic substorms [30,36,68]. The heating that results from Joule dissipation also makes it a likely candidate that could account for the million-degree temperatures observed to characterize the solar corona [53,20,48]. The ubiquitous nature of reconnection may be understood as a manifestation of the tendency for fields in a close-to-ideal MHD regime to spontaneously develop TDs. In particular, analytical studies show that the topology of continuous fields in a static equilibrium (i.e. for which $-\nabla\pi' + \nabla \cdot (\mathbf{B}\mathbf{B})/(\mu_0\rho_0) = 0$ in (32)) is not compatible, in general, with that of an arbitrary, non-equilibrium configuration [34]. The only way for the system to attain such an equilibrium is therefore to modify its topology by means of reconnection.

Under the frozen-in condition, TD formation may be captured by following

the evolution of pairs of flux surfaces, collectively represented by sets of level surfaces $S_1(\mathbf{x}, t)$ and $S_2(\mathbf{x}, t)$, also called Euler potentials

$$DS_1/Dt = 0 , \tag{60}$$

$$DS_2/Dt = 0 . \tag{61}$$

Since the field is tangent to the flux surfaces, it must be everywhere parallel to their intersection

$$\mathbf{B} = W(S_1, S_2) \nabla S_1 \times \nabla S_2 , \tag{62}$$

where $W(S_1, S_2)$ controls the field amplitude. Together with (62), (60) and (61) completely determine the evolution of \mathbf{B} [1]. However, the possibility of infinitely long field lines or torsion limits the description in terms of Euler potentials to the case of zero magnetic helicity

$$\mathfrak{H} \equiv \int_{\Omega} \mathbf{A} \cdot \mathbf{B} dV = 0 , \tag{63}$$

where \mathbf{A} is the magnetic vector potential [1,41].

Here we will assess the impact of the MA correction on the evolution of a relaxing magneto-fluid by solving (32)-(35). In this system, total energy decreases monotonically as the viscous force drags the fluid toward a state of minimum magnetic energy with $\mathbf{v} = 0$ (i.e. the total energy rate-of-change $\chi = d\mathcal{E}/dt \leq 0$) [1]. Moreover, the finite resistivity that is necessary to achieve topological change must arise from the truncation terms of numerical approximations (38). The initial condition for the velocity and magnetic field are given by $\mathbf{v} = 0$ and (62) with $S_1 = \cos(y)^2 \sin(x)$, $S_2 = z$ and $W = 1$. In addition to (32)-(35), (60) and (61) are integrated in time and space as $S_j^n = LE_i(\widehat{S}_j)$, $j = \{1, 2\}$ to recover the Euler potentials, which are useful for the identification of TDs. This approach obviates the need to integrate \mathbf{B} to obtain S_1 and S_2 and therefore eliminates errors that come along with such a procedure. Although the approach consisting of (60), (61) and (62) could be used as an alternative to the algorithm exposed in section 3, it is less general than the latter and involves errors of its own, e.g. see [7]. However, in the present context it provides a convenient means of assessing the uncertainty of numerical solutions and the enforcement of the frozen-in condition, as will be shown shortly.

Before the start of each simulation, the field resulting from the finite-difference operators used to evaluate (62), which is denoted by \mathbf{B}_a , undergoes divergence cleaning through the elliptic problem for π^* : $\nabla \cdot \mathbf{B} = \nabla \cdot (\mathbf{B}_a - \nabla \pi^*) = 0$ to ensure the discrete form of (35) to a round-off error. The pressure perturbation π' is set to zero initially, thereby setting up an imbalance in (32), (i.e. $-\nabla \pi' + \nabla \cdot (\mathbf{B}\mathbf{B})/(\mu_0 \rho_0) \neq 0$). We shall describe the system's evolution using the non-dimensional time $t^* = t/t_A$, where t is simulated physical time and $t_A \equiv$

$2\pi/v_A \approx 6.28s$ is the typical time it takes for a magnetic disturbance to cross the system, also called dynamical time. Here $v_A = (B_0/\sqrt{\mu_0\rho_0})$ is the Alfvén velocity and $B_0 = 1T$ is the maximal strength of the initial field. The timestep size is $\Delta t = 8 \times 10^{-3}s$ or, equivalently, 1.27×10^{-3} dynamical times, which is five times smaller than the maximal timestep required for the stability of viscous dissipation and 15 times smaller than the timescale of reconnection (based on the shortest timescale of magnetic energy release in a reconnection event from our 2D experiments). We begin by considering a 2D setup and then move on to 3D analogs of the same experiment.

5.1 2D magneto-fluid

Analyzed in this section are an uncorrected classical SL and a MA-enhanced solution using $\varepsilon = 1 \times 10^{-2}$ in (52), both of which employ a second-order-accurate trajectory scheme. The domain is a doubly-periodic square box of size $[-\pi, \pi] \times [-\pi, \pi]$ and a uniform grid resolution $NX = NY = 256$ is used.

Figure 6 shows the magneto-fluid at various times during its evolution for the experiment using the MA trajectory correction. Each panel displays isolines of the Euler potential S_1 (white lines), which are superposed over a color map of the vertical component of the current density (j_z). Since the fluid is 2D, the isolines can be identified with individual magnetic field lines as long as the frozen-in condition holds to a satisfactory degree. Black arrows show randomly selected magnetic field lines constructed from the prognosed field and indicate the sense of \mathbf{B} . The alignment between isolines and random field lines therefore provides a measure of the enforcement of the frozen-in condition.

The initial state at $t^* = 0$ (upper-left panel) consists of six sub-systems of closed field lines, or ‘magnetic islands’. Islands to the left of the $x = 0$ axis have counterclockwise oriented field lines and therefore a positive current density pointing into the plane of the figure at their center, whereas; those to the right have a clockwise orientation and a corresponding negative current density. This state is unstable as a result of its unbalanced magnetic stresses and so it will seek an equilibrium in which the balance of forces is met. At $t^* = 5.6$ (upper-right panel), the islands already have contracted horizontally and expanded vertically so that they now press against each other across the former neutral lines at $y = \pm 0.5\pi$. Observe that the horizontal component of \mathbf{B} abruptly changes sign across those two lines and that CSs have formed in these regions, also called magnetic X-points, which have been labelled by letters a,b,c and d. In particular, the level curves $S_1 = \pm 0.0345$, which used to represent closed field lines at $t^* = 0$, now extend from $y = -\pi$ to $y = +\pi$ as a result of their reconnection across the $y = \pm 0.5\pi$ lines. TDs appear here as cusps in the isolines where the field lines are non-differentiable. This quasi-

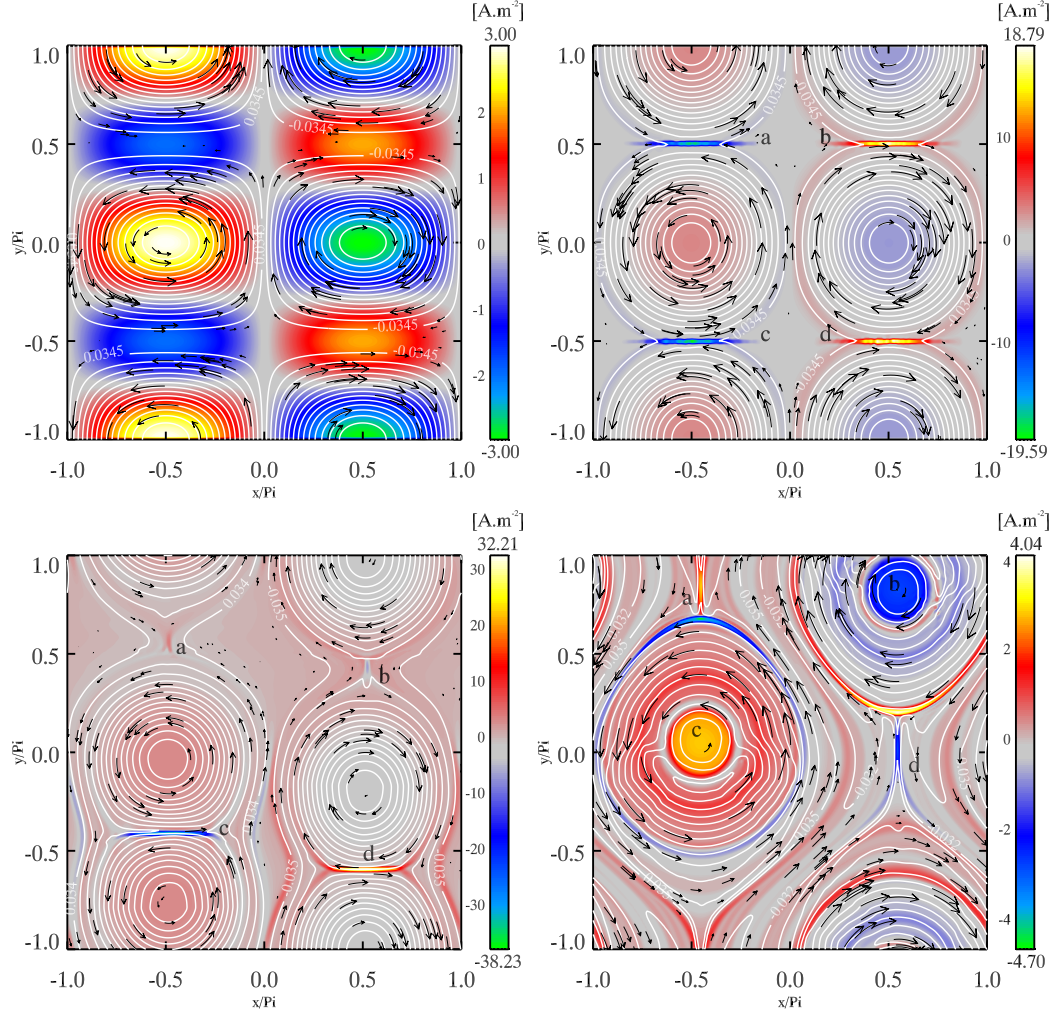


Fig. 6. Relaxation of a magneto-fluid into equilibrium. Each panel shows a color map of the vertical component of the current density, over which are superposed isolines of the Euler potential S_1 along with randomly selected magnetic field lines (arrows). The upper-left panel shows the initial (un-balanced) condition. Other panels correspond to snapshots taken at non-dimensional times $t^* = 5.6$ (top-right), $t^* = 12.74$ (bottom-left) and $t^* = 51$ (bottom-right). Note the widely differing ranges of scales of the current density in all four panels.

static flow configuration (or quasi-static state) persists until $t^* \approx 10$, when it finally destabilizes as islands on each side of CSs at (c) and (d) are propelled towards each other by the tension of the reconnected field lines and begin merging into larger structures — see the lower-left panel of fig. 6 ($t^* = 12.74$). Only three subsystems out of six remain at $t^* = 51$, where the system appears to have attained another quasi-static state — see the lower-right panel of fig. 6. Apart from slight misalignments between isolines and field lines taking place close to the O-shaped current-carrying regions at (c) and (b) in the final state, the agreement between the field predicted from the Euler potentials and the one obtained from the integration of (32)-(35) throughout the rest of the evo-

lution is remarkable. The process depicted by fig. 6 and by which reconnected field lines evolve from the harmonic into the subharmonic mode is known as the coalescence instability and has been widely studied both analytically and numerically [19,55,50].

Histories of the normalised total kinetic energy (KE) and total magnetic energy (ME) corresponding to the time sequence displayed in figure 6 appear in the top panel of figure 7, where they are displayed by black and red curves, with continuous and dotted curves corresponding to runs using the classical SL and MA-enhanced algorithms, respectively. The panel immediately below shows the total energy rate-of-change χ , where black continuous and red dotted curves correspond to the standard SL and MA-enhanced SL runs. The KE first increases from zero to reach approximately 4% of the total initial ME as the islands are set into motion and as X points are formed, only to fall back down near zero around $t^* \approx 3$ under the action of the viscous force. This period is characterized by a magnetic back-reaction causing a short feedback of KE into ME. The latter is not the result of reconnection but rather is the effect of an Alfvén wave propagating throughout the domain; see the animation in the supplementary material online. Notably, both solutions remain identical until the quasi-static state is reached at $t^* \approx 3$, when a KE burst associated with $\chi > 0$ (i.e. an increase of the total energy \mathcal{E}) appears for the first time — see the insets showing a close-up view of the interval $\langle 2, 4 \rangle$. The latter therefore clearly is a non-ideal effect that can be attributed to a reconnection event taking place at a magnetic X point. KE bursts keep occurring during the quasi-static state until the onset of the merging process at $t^* \approx 10$, during which more than 30% of both solutions’ total ME is converted into KE. Remarkably, violations of $\chi \leq 0$ are about 10 times larger in the standard than in the MA-enhanced run during the merging phase and those are much more frequent when the MA correction is not applied. In the MA-enhanced solution, the KE is almost completely dissipated by viscous forces to produce the quasi-static state at $t^* \approx 50$. This is not the case for the classical SL run, however, in which both KE and ME start to increase unboundedly past $t^* \approx 22$, dramatically violating conservation of the total energy. Consequently, the standard SL run was terminated shortly after $t^* \approx 24$.

The third panel of figure 7 shows the histories of cross-helicities

$$H \equiv \int_{\Omega} \mathbf{v} \cdot \mathbf{B} dV , \quad (64)$$

associated with the standard SL (continuous curve) and MA-enhanced solutions (dotted curve). Cross-helicity is an invariant of ideal MHD without dissipation that provides a measure of linkage between vortex and magnetic field lines [44]. Since $\mathbf{v} = 0$ initially, departures from $H = 0$ indicate changes in the flow/field topology that are either due to reconnection or viscous losses. The inset indicates that the first departure coincides with the KE burst at-

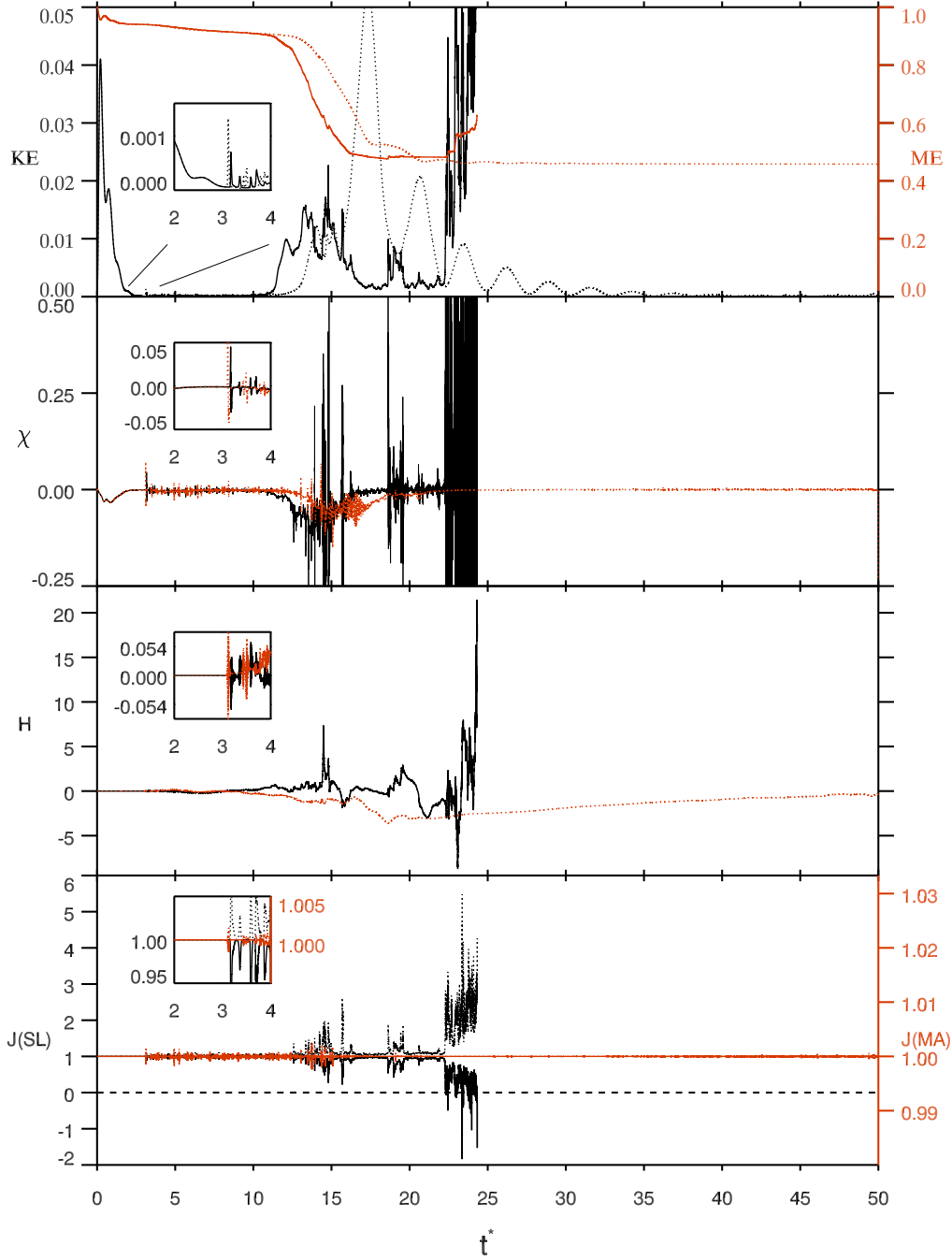


Fig. 7. Top: Kinetic energy (black) and magnetic energy (red) for the classical SL solution (continuous) and for the MA-enhanced solution (dots). 2nd panel from the top: Total energy rate-of-change for standard (black continuous line) and MA-enhanced runs (red dots). 3rd panel from the top: Cross-helicity for the classical SL (black continuous) and MA-enhanced solutions (red dots). Bottom panel: Minimum (continuous) and maximum of \hat{J} (dots) for the classical SL (black) and MA-enhanced solutions (red). The time axis is non-dimensional time t^* .

tributed to the first reconnection event at $t^* \approx 3$. Both MA-enhanced and classical SL solutions compare well during the quasi-static state prior to $t^* \approx 10$; whereas, they begin to diverge past this time as the island coalescence takes its course. This phase is characterized by large fluctuations in the classical SL solution, the most dramatic being the erratic growth seen to occur in the interval $t^* \in \langle 22, 24 \rangle$ and simultaneously with the spurious generation of ME — compare with the top panel. Fluctuations and departures from $H = 0$ occurring in the MA-enhanced run are, on the other hand, much more tempered.

Histories of $\min\{\hat{J}\}$ and $\max\{\hat{J}\}$ are displayed by solid and dotted curves for the classical SL (black curves) and MA-enhanced solutions (red curves) in the bottom panel of figure 7, respectively. A dashed line has been drawn that marks the ordinate where $\hat{J} = 0$ on the scale of the classical SL solution. As it was the case for H , the largest departures from (8) are observed during the coalescence phase, with the classical SL solution exhibiting singular mappings ($\hat{J} \leq 0$) as its magnetic energy starts to grow spuriously. The MA-enhanced solution, on the other hand, shows departures from (8) no greater than 1% throughout the whole evolution.

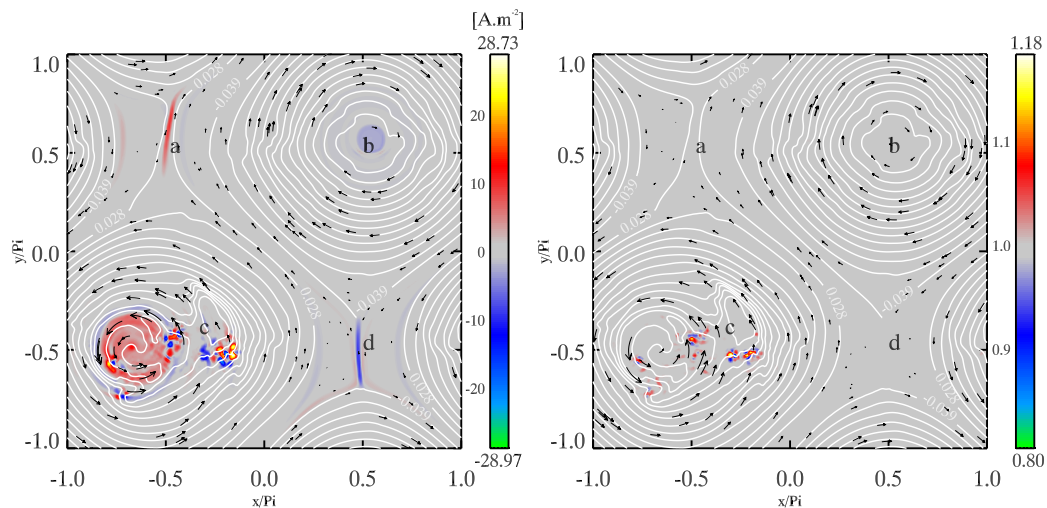


Fig. 8. Anomalous fluid expansion and contraction in a classical SL solution at $t^* = 24$, immediately before its termination. Left and right snapshots show, respectively, S_1 isolines superposed over a color map of the j_z and a color map of \hat{J} .

Left and right panels of figure 8 show, respectively, snapshots of S_1 isolines superposed over color maps of j_z and \hat{J} immediately before the termination of the classical SL run at $t^* = 24$. Although islands appear to have merged as in the MA-enhanced solution, field lines pertaining to the bundle at (c) are quite distorted and the alignment between the isolines of S_1 and the field lines is lost. Interestingly, the intense and spatially complex current distribution observed at (c) in the left panel corresponds to the region where the largest \hat{J}

errors appear (right panel). Those errors can be attributed to both anomalous contraction ($\hat{J} > 1$) and anomalous expansion ($\hat{J} < 1$).

5.2 3D magneto-fluid

The fact that most natural systems evolve in more than two space dimensions demands further assessment of the MA-enhanced scheme in a 3D environment. Hence, we further explore its comparison with the classical SL scheme using 3D analogs of the experiments of section 5.1. Here the domain is a triply-periodic box $[-\pi, \pi] \times [-\pi, \pi] \times [0, \pi/4]$ with grid resolution $NX = NY = 256$, $NZ = 32$ and initial conditions are given as before by $\mathbf{v} = 0$, (62), $S_1 = \cos(y)^2 \sin(x)$, $S_2 = z$, $W = 1$. Thus, field lines at $t^* = 0$ all lie in horizontal planes with the configuration shown in the top-left panel of figure 6. We begin by comparing results from second-order-accurate uncorrected and corrected trajectory schemes. The MA-enhanced run uses $\varepsilon = 1 \times 10^{-2}$ in (52).

The upper graph of figure 9 shows histories of the KE and of the ratio of volume-integrated vertical ME to total ME ($\langle B_z^2 \rangle / \langle \mathbf{B}^2 \rangle$) for the first 10 dynamical times of each run. The lower graph shows, snapshots of field lines in the region $-\pi < x, y < 0$ for standard SL (top panels) and MA-enhanced runs (bottom panels) at various times during their evolution (from left to right). As in the 2D solution, KE initially grows out from the instability that leads to the formation of the four X-points and a quasi-static state; see the two leftmost snapshots in the lower graph. Here, however, an infinitesimal but non-zero amount of ME lies in the vertical magnetic field at $t^* = 0$ as a result of the enforcement of (35) for the initial condition. The latter eventually settles into a phase of exponential increase that lasts until $t^* \approx 3$, when a first KE burst appears due to reconnection, causing it to jump by several orders of magnitude almost instantaneously. Notably, the first reconnection event occurs at the same instant as in the 2D runs at $t^* \approx 3$, prior to which the flow evolution is purely 2D, with only a billionth of the total ME residing in B_z . Profuse liberation of ME into KE takes place shortly after, only to be dissipated away by viscous forces. The growth of the main KE peak at $t^* \approx 5$ is accompanied by significant build up of vertical ME that shows up as kinking of the field lines in the central regions of the islands — see central panels of the lower graph, corresponding to $t^* = 5.09$. By $t^* = 10$, the vertical magnetic field contains $\approx 15\%$ of the total ME and the field itself has become chaotic, as shown by the two rightmost panels. Thus, the growth of B_z overwhelms the 2D state before the islands can complete merging together and, as a result, the state of the 3D solution at $t^* = 10$ is very different from the one obtained at $t^* = 51$ in the 2D experiments — compare with the bottom-right panel of fig. 6.

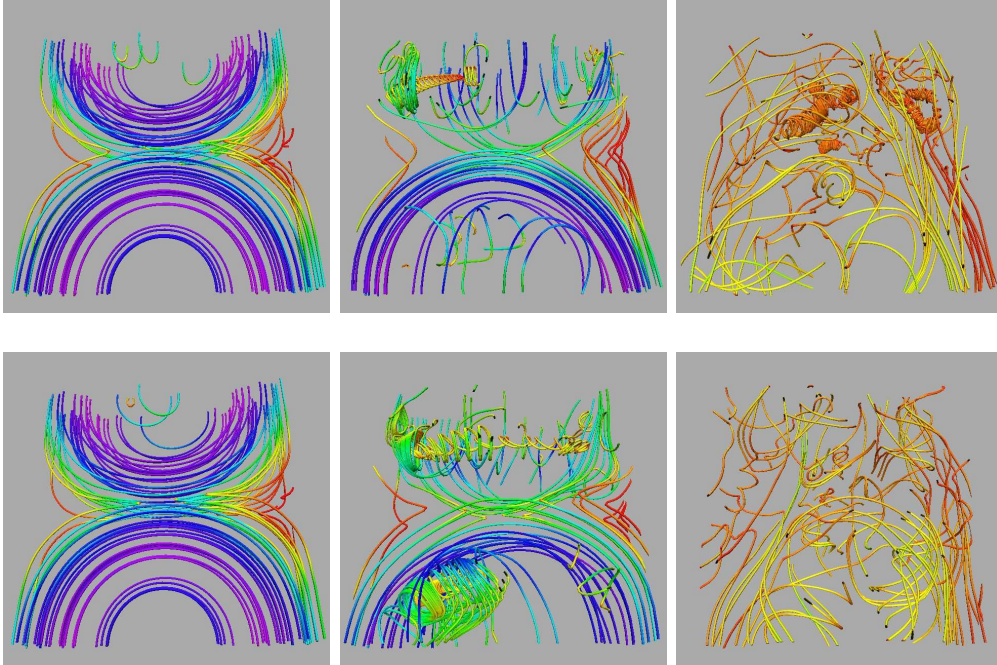
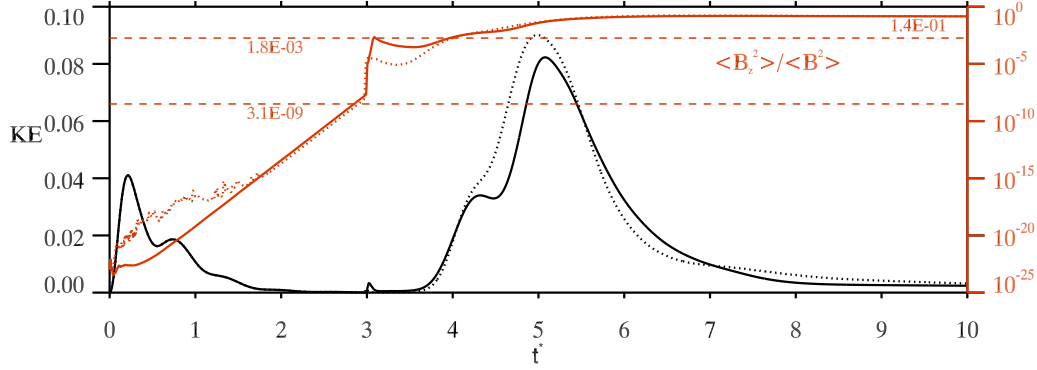


Fig. 9. Top graph: Kinetic energy (black curves) and ratio $\langle B_z^2 \rangle / \langle \mathbf{B}^2 \rangle$ (red curves) histories for the classical SL solution (continuous curves) and for the MA-enhanced solution (dots). Lower graph: color rows show consecutive snapshots of the magnetic field lines in classical SL (top) and MA-enhanced runs (bottom) taken at, respectively, $t^* = 3.82$, $t^* = 5.09$ and $t^* = 10.19$.

Noteworthy, experiments that have been studying the growth of 3D modes starting from a 2D static equilibrium containing magnetic islands also report a diminished role of the coalescence instability [19]. In particular, 3D modes are observed to grow faster than any of the 2D modes associated with the relaxation of the reconnected field into the subharmonic mode and so field lines move out of their respective planes quicker than they reconnect, thereby preventing the merging of the islands.

Histories of cross-helicity H (64) and the current helicity

$$H_c \equiv \int_{\Omega} (\nabla \times \mathbf{B}) \cdot \mathbf{B} dV , \quad (65)$$

are shown in the top panel of figure (10) with black and red curves, respectively. Unlike H , H_c is not an MHD invariant and instead gives a measure of torsion in the field lines. Both quantities are well conserved for the classical SL (solid curve) and MA-enhanced run (dotted curve) prior to the onset of reconnection. However, jumps appear in their evolution in the classical SL run which coincide with the first KE burst — see the inset showing a magnification of interval $t^* \in \langle 2.8, 4 \rangle$. Those jumps are, on the other hand, smaller in amplitude by at least an order of magnitude in the MA-enhanced run. Moreover, H grows linearly at a higher rate in the classical SL than in the MA-enhanced run during the dynamical time following $t^* \approx 3$. In contrast, nothing precise can be said about the behavior of both schemes with respect to conservation of both quantities past $t^* \approx 4$ as the flow becomes chaotic. Histories of $\min\{\hat{J}\}$ and $\max\{\hat{J}\}$ for the classical (black curves) and MA-enhanced runs (red curves) are shown in the bottom panel. Observe that the largest errors take place in the classical SL run simultaneously with the large jumps in H and H_c at $t^* \approx 3$. Notably, departures from $\hat{J} = 1$ only appear during the brief interval $t^* \in \langle 3, 5 \rangle$ and diminish as the flow transits toward a 3D configuration and a chaotic state. By contrast, they persisted over a much longer period of time in the 2D experiments, in which reconnection kept on going for several dynamical times as a result of island coalescence; cf. bottom panel of fig. 7.

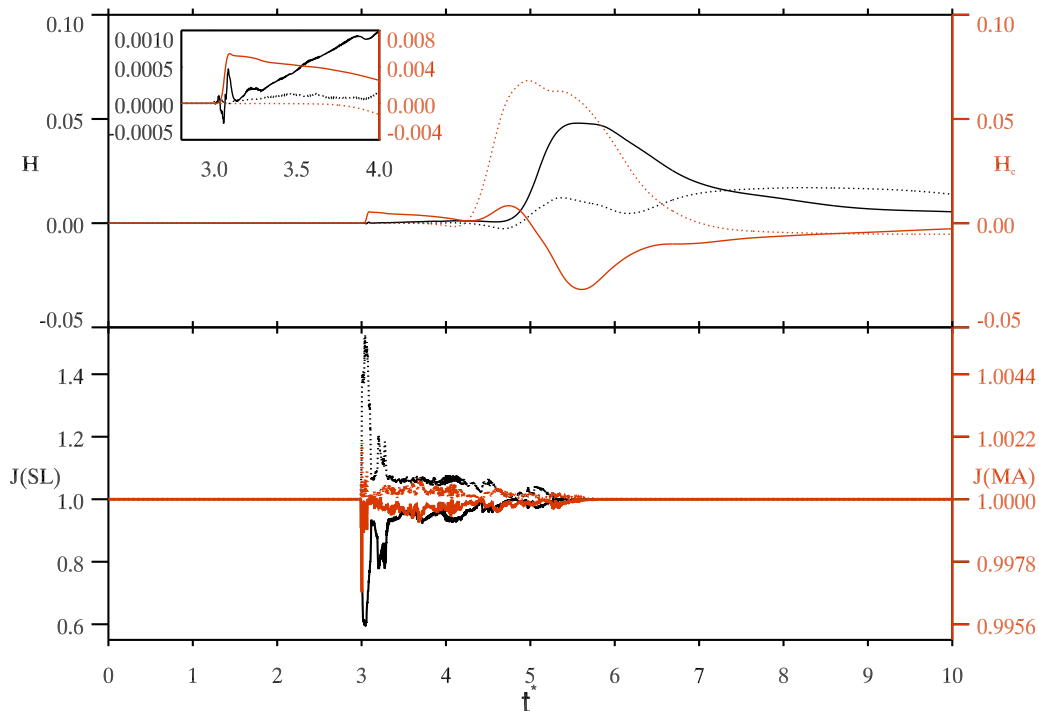


Fig. 10. Top: Cross-helicity (black curves) and current helicity histories (red curves) for the classical SL (continuous curve) and MA-enhanced solutions (dotted curve). Bottom: Histories of minimum (continuous lines) and maximum (dots) of the (time-independent) inverse flow Jacobian taken over the computational grid for the classical SL (black curves) and MA-enhanced solutions (red curves).

Table 3 provides a quantitative measure of fluctuations of H and H_c occurring at the beginning of the brief reconnection phase by displaying total time variations $\Delta H \equiv \int |dH/dt| dt$ and $\Delta H_c \equiv \int |dH_c/dt| dt$. Using timeseries data of H and H_c , we computed $\delta H \equiv \sum_i |H_{i+1} - H_i|$ and $\delta H_c \equiv \sum_i |(H_c)_{i+1} - (H_c)_i|$ for the interval $t^* \in \langle 2.8, 4 \rangle$ for runs that employ various accuracies of the inverse flow Jacobian. The first column identifies each run, with an integer

SL run	$\delta H [\times 10^3]$	$\delta H_c [\times 10^3]$	t/t_{standard}
0	4.66	8.40	1.00
1	1.74	0.96	0.97
2	2.55	1.27	1.03
3	2.52	0.51	1.27
4	2.53	0.54	1.68

Table 3

Sensitivity to Jacobian residual and performance of the 3D solver. The first column identifies the experiment, where the integer denotes the base-10 logarithm of the MA solver convergence threshold ε . Second and third columns display the time variations δH and δH_c for the interval $t^* \in \langle 2.8, 4 \rangle$, while the last column indicates the total wallclock time normalized with respect to the standard SL scheme.

corresponding to the base-10 logarithm of ε . The normalized time-to-solution (wallclock time) relative to the standard SL run t/t_{standard} is displayed in the last column. The classical SL experiment (run 0) indeed possesses the largest of all variations. In particular, δH appears to converge to a value $\delta H \approx 2.5$ after the residual has been decreased by 2 orders of magnitude; whereas δH_c converges to $\delta H_c \approx 0.5$ after a 3 orders-of-magnitude decrease.

Fluctuations of H and H_c taking place for $t^* > 4$ are, by opposition, far greater and are especially strong during the growth of B_z and transition to chaos; see the central panels of both solutions in the lower graph of fig. 9. The fact that no systematic impact due to the use of the MA correction can easily be discerned from histories of H and H_c in this time period either points to interpolation errors smearing out the effect of the trajectory correction (recall the discussion in the last paragraph of section 4) or simply to the chaotic flow behavior that prevails past $t^* \approx 4$.

Noteworthy, discrepancies in the current-helicities predicted by corrected and uncorrected schemes will manifest themselves as differing amounts of twist in fields of both solutions. This would appear to be consistent with the observed differences between the morphologies of field lines from each run (fig. 9)

6 Summary

We studied the impact of incompatible integrations of the equations of incompressible fluid and magneto-fluid dynamics using the semi-Lagrangian approximation. A necessary condition for the compatibility of a SL scheme has been defined through the solution of (8) using the fundamental Euler expansion formula and the mass continuity equation. Closed-form solutions to the MAEs arising from purely rotational and deformational elemental flows have shown that the anomalous contraction and expansion resulting from Euler-forward trajectory approximations to the trajectory integrals (3) are eliminated by the MA trajectory correction. Scalar advection experiments using the MA correction support the theoretical results from section 2 by removing a substantial part of the anomalous contraction introduced by the standard trajectory estimates and by improving mass conservation.

Magnetic relaxation experiments have provided an extreme example where the consequences of breaking the flow topology and neglecting to enforce (8) altogether can be disastrous to the numerical solution. In particular, enforcing (8) has proven to be crucial for assuring the physical realizability and nonlinear stability of the 2D experiments, in which the lack of MA correction lead to unbounded growth of the total energy and trajectory intersections. Applying the MA correction in 2D and 3D experiments further has improved the conservation of the cross-helicity MHD invariant during phases of reconnection.

Future studies of the impact of compatibility on the flow features could be extended to stratified flows in more complex geometries (with suitable boundary conditions) by deriving corresponding generalized MAEs from (6), such as, for instance, global MHD simulations of the solar convection zone [14,5,52,29].

Acknowledgments

We would like to thank three anonymous referees for their comments, which helped to improve the presentation. The numerical simulations reported in this paper were carried out primarily on the computing facilities of Calcul Québec, a member of the Compute Canada consortium. This work is supported by Canada's Foundation for Innovation, Natural Sciences and Engineering Research Chair program and Discovery Grant program (PC), and the NSERC Graduate Fellowship Program (JFC). PKS acknowledges support by funding received from the European Research Council under the European Union's Seventh Framework Programme (FP7/2012/ERC Grant agreement no. 320375).

Appendix A: Ellipticity of the 2D MAE

Let Ω be a convex domain in which the MAE solution is sought and $\partial\Omega$ its boundary. A nonlinear PDE in M variables of the form

$$P(x_1, \dots, x_M, \phi, \phi_1, \dots, \phi_{MM}) = 0, \quad (66)$$

is said to be elliptic if the quadratic form

$$\sum_{i,k=1}^M \frac{\partial P}{\partial \phi_{ik}} \theta_i \theta_k, \quad (67)$$

is positive definite in the parameters θ for all x_1, x_2, \dots, x_M in Ω and all values of the other arguments of P (cf. section IV.6.2 of [16]); here $\phi_i \equiv \partial\phi/\partial x_i$ and $\phi_{ik} \equiv \partial^2\phi/\partial x_i\partial x_k$. Therefore, the quadratic form associated to (12) may be expressed as

$$Q(\theta_1, \theta_2) \equiv (E\phi_{yy} + A)\theta_1^2 - 2(E\phi_{xy} - B)\theta_1\theta_2 + (E\phi_{xx} + C)\theta_2^2, \quad (68)$$

and is positive-definite provided $(\theta_1, \theta_2) = (0, 0)$ is a minimum. This is the case if the discriminant $\Lambda \equiv 0.25(Q_{\theta_1\theta_1}Q_{\theta_2\theta_2} - Q_{\theta_1\theta_2}^2) > 0$, $Q_{\theta_1\theta_1} > 0$ and $Q_{\theta_2\theta_2} > 0$. Using (12), we find that the condition for ellipticity is given by

$$\Lambda = (E\phi_{yy} + A)(E\phi_{xx} + C) - (E\phi_{xy} - B)^2 = AC - B^2 - DE > 0, \quad (69)$$

and

$$E\phi_{xx} + C > 0, \quad E\phi_{yy} + A > 0. \quad (70)$$

On the other hand, a negative-definite Q is defined by $\Lambda > 0$, $Q_{\theta_1\theta_1} < 0$ and $Q_{\theta_2\theta_2} < 0$, which implies

$$E\phi_{xx} + C < 0, \quad E\phi_{yy} + A < 0. \quad (71)$$

Importantly, Q is either positive-definite or negative-definite given (69), whereby ϕ must fall into either one of the two solution classes defined by (70) and (71). For the special case where $A = B = C = D = 0$, (70) and (71) imply, respectively, convexity and concavity of the MAE solution ϕ , whereby (12) is elliptic if and only if ϕ is convex [27,4]. In general, however, one cannot expect the MAE solution to be either convex or concave. Consequently, in this paper we shall simply refer to solutions satisfying (70) and (71) as the type-1 and type-2 solutions. Hence, (12) is elliptic if and only if ϕ is a type-1 solution.

To obtain an interpretation of (69) in terms of fluid flow, we substitute (13) into (69), and express the latter in terms of the derivatives of the path-mean velocity $\tilde{\mathbf{v}}$. This leads readily to $\Lambda = 1 - (0.5\Delta t(\tilde{u}_y - \tilde{v}_x))^2 = 1 - (0.5\Delta t\tilde{\omega})^2 > 0$,

whereupon

$$\left| \frac{\tilde{\omega}\Delta t}{2} \right| < 1 \quad (72)$$

becomes both the necessary and sufficient condition for (69). Furthermore, the inequality (72) is closely linked to the Lipschitz condition

$$L := \Delta t \left\| \frac{\partial \tilde{\mathbf{v}}}{\partial \mathbf{x}} \right\| < 1, \quad (73)$$

which gives a measure of convergence/divergence of the estimated flow trajectories (9) and suffices for preventing their intersections, where the velocity field is assumed to be at least $C^{(1)}$ [58]. Now, rearranging (73) gives

$$\begin{aligned} 1 > L &:= \Delta t (|\tilde{v}_x| + |\tilde{u}_y| + |\tilde{v}_y| + |\tilde{u}_x|) \\ &\geq \Delta t (|\tilde{v}_x - \tilde{u}_y| + |\tilde{v}_y| + |\tilde{u}_x|) \\ &\geq \Delta t |\tilde{v}_x - \tilde{u}_y| \\ &\geq 0.5\Delta t |\tilde{v}_x - \tilde{u}_y| = 0.5\Delta t |\tilde{\omega}|. \end{aligned} \quad (74)$$

Thus, $L < 1$ is sufficient for (72) and therefore also (69).

Appendix B: Unicity of MAE solutions

To determine the unicity of solutions to (12), one must have some knowledge of the imposed boundary conditions. For instance, the Dirichlet problem for the MAE consists in finding a solution to (12) in a domain Ω with specified solution at the boundary $\partial\Omega$, e.g. $\phi|_{\partial\Omega} = \Gamma$, where Γ is a known function of the coordinates. At most two solutions to the Dirichlet problem exist, which assume the same boundary values Γ , given the non-negative discriminant (14). This result, known as the Rellich theorem, follows from the demonstration that for specified Γ the type-1 and type-2 solutions are unique (cf. appendix A and section IV.6.3 of [16]). For example, it is possible to choose the constants C_+ and C_- in (23) such that $F_+(\xi^*) \equiv F_-(\xi^*) = \Gamma$ on a circle of radius $R = \sqrt{\xi^*}$ centered at the origin, whereby F_+ and F_- are unique for a given Γ .

Moreover, for arbitrary boundary conditions, a solution to (12) is either type-1 or type-2 if (14) is satisfied, although the authors know of no corresponding proof of uniqueness. In such a case, however, the type of solution can be verified once a particular solution has been found, for instance with the use of a numerical solver; see sections 3.2 and 4.

Substituting (13) in the left inequalities of (15) and (16) implies, respectively,

$$\Delta t \phi_{xx}^{\{1\}} > \Delta t \tilde{u}_x - 1 \geq -\Delta t |\tilde{u}_x| - 1 > -L - 1 > -2 \quad (75)$$

and

$$\Delta t \phi_{xx}^{\{2\}} < \Delta t \tilde{u}_x - 1 \leq \Delta t |\tilde{u}_x| - 1 < L - 1 < 0, \quad (76)$$

where $\phi_{xx}^{\{1\}}$ and $\phi_{xx}^{\{2\}}$ correspond to the type-1 and type-2 solutions. Similarly, $\phi_{yy}^{\{1\}} > -2/\Delta t$ and $\phi_{yy}^{\{2\}} < 0$. This last property imposes severe constraints on solutions of the second type, namely, that they possess only one stationary point (a maximum).

If periodic boundary conditions are assumed for all prognosed dependent variables the trajectory correction, $\nabla\phi$, in (11) must also be periodic, whereupon one has the additional constraint

$$0 = \phi_x|_X - \phi_x|_0 = \int_0^X \phi_{xx}, \quad (77)$$

and similarly for ϕ_{yy} . This clearly forbids the existence of type-2 solutions, as per inequality (76) and the associated upper bound on ϕ_{yy} .

The above argument can also be applied to a bounded domain Ω , since in this case one would have $\phi_x|_0 = \phi_x|_X = 0$ in (77) as a result of prescribing zero normal velocity on $\partial\Omega$. In this situation, observing (17) would also assure that the departure points remain inside the domain, since fluid elements from its interior could not leave Ω without intersecting trajectories of the elements moving alongside $\partial\Omega$. Generally, for problems with the normal components of the trajectory displacements specified at the domain boundary, boundary conditions for (12) may be derived from (11), which naturally leads to a Neumann problem for the MAE [3,21,66,64].

References

- [1] R. Bhattacharyya, B.C. Low, P.K. Smolarkiewicz, On spontaneous formation of current sheets: Untwisted magnetic fields, *Phys. Plasmas* 17 (2010) 112901.
- [2] J.D. Benamou, Y. Brenier, A computational fluid mechanics solution to the Monge-Kantorovich mass transfer problem, *Numer. Math.* 84 (2000) 375-393.
- [3] J.D. Benamou, B.D. Froese, A.M. Oberman, Numerical solution of the optimal transportation problem using the Monge-Ampère equation 260 (2014) 107-126.
- [4] J.D. Benamou, B.D. Froese, A.M. Oberman, Two numerical methods for the elliptic Monge-Ampère equation, *ESAIM: Math. Model. Numer. Anal.* 44 (2010) 737-758.
- [5] P. Beaudoin, P. Charbonneau, É. Racine, P.K. Smolarkiewicz, Torsional oscillations in a global solar dynamo, *Sol. Phys.* 282 (2013) 335-360.
- [6] C.P. Boyer, P. Winternitz, Symmetries of the Self-Dual Einstein equations. 1. The infinite dimensional symmetry group and its low-dimensional subgroups, *J. Math. Phys.* 30 (1989) 1081-1094.

- [7] A. Brandenburg, Magnetic field evolution in simulations with Euler potentials, *Mon. Not. R. Astron. Soc.* 401 (2010) 347-354.
- [8] Y. Brenier, Polar factorization and monotone rearrangement of vector-valued functions, *Comm. Pure. Appl. Math.* 44 (1991) 375-417.
- [9] P.N. Brown, Y.S. Saad, Hybrid Krylov methods for nonlinear systems of equations, *SIAM J. Sci. Stat. Comput.* 11 (1990) 450-481.
- [10] C.J. Budd, J.F. William, Moving mesh generation using the parabolic Monge-Ampère equation, *Siam J. Sci. Comput.* 31 (2009) 3438-3465.
- [11] C.J. Budd, M.J.P. Cullen, E.J. Walsh: Monge-Ampère based moving mesh methods for numerical weather prediction, with applications to the Eady Problem, *J. Comput. Phys.* 236 (2013) 247-270.
- [12] A.J. Chorin, J.E. Marsden, *A mathematical introduction to fluid mechanics*; 3rd. ed., Springer-Verlag, New York, 1993.
- [13] J.N. Clelland, T.A. Ivey, Parametric Bäcklund transformations I : Phenomenology, *Trans. Amer. Math. Soc.* 357 (2004) 1061-1093.
- [14] J-F. Cossette, P. Charbonneau, P.K. Smolarkiewicz, Cyclic thermal signature in a global MHD simulation of the solar convection zone, *ApJL*, 777 (2013) L19.
- [15] J-F. Cossette, P.K. Smolarkiewicz, A Monge-Ampère enhancement for semi-Lagrangian methods, *Comput. Fluids* 46 (2011) 180-185.
- [16] R. Courant, D. Hilbert, *Methods of Mathematical Physics*, Vol. 2, Wiley-VCH, Mörlenbach, 1962.
- [17] M.J.P. Cullen, R.J. Douglas, I. Roulstone, M.J. Sewell, Generalized semi-geostrophic theory on a sphere, *J. Fluid. Mech.* 531 (2005) 123-157.
- [18] M.J.P. Cullen, J. Norbury, R.J. Purser, Generalised Lagrangian solutions for atmospheric and oceanic flows, *SIAM J. Appl. Math.* 51 (1991) 20-31.
- [19] R.B. Dahlburg, G. Einaudi, MHD unstable modes in the 3D evolution of 2D MHD structures and the diminished role of coalescence instabilities, *Phys. Lett. A* 294 (2002) 101-107.
- [20] R.B. Dahlburg, J.A. Klimchuk, S.K. Antiochos, An explanation for the ‘switch-on’ nature of magnetic energy release and its application to coronal heating, *ApJ* 622 (2005) 1191-1201.
- [21] G.L. Delzanno, L. Chacón, J.M. Finn, Y. Chung, G. Lapenta, An optimal robust equidistribution method for two-dimensional grid adaptation based on Monge-Kantorovich optimization, *J. Comput. Phys.* 227 (2008) 9841-9864.
- [22] D.G. Dritschel, Á. Viúdez, A balanced approach to modelling rotating stably stratified geophysical flows, *J. Fluid. Mech.* 488, (2003) 123-150.
- [23] S.C. Eisenstat, H.C. Elman, M.H. Schultz: Variational iterative methods for nonsymmetric systems of linear equations, *SIAM J. Numer. Anal.* 20 (1983) 345-357.

- [24] M. Falcone, R. Ferreti, Convergence analysis for a class of high-order semi-Lagrangian advection schemes, *SIAM J. Numer. Anal.* 35 (1998) 909-940.
- [25] E.V. Ferapontov, Y. Nutku, On the Monge-Ampère equivalent of the sine-Gordon equation, *J. Phys. A: Math. Gen.* 27 (1994) 7831-7834.
- [26] V.C.A. Ferraro, C. Plumpton, *An introduction to magneto-fluid mechanics*, Clarendon P., Oxford, 1966.
- [27] B.D. Froese, A.M. Oberman, Fast finite difference solvers for singular solutions of the elliptic Monge-Ampère equation, *J. Comput. Phys.* 230 (2011) 818-834.
- [28] X. Garbet, Y. Idomura, L. Villard, T.H. Watanabe, Gyrokinetic simulations of turbulent transport, *Nucl. Fusion* 50, 2010.
- [29] M. Ghizaru, P. Charbonneau, P.K. Smolarkiewicz, Magnetic cycles in global large-eddy simulations of solar convection, *ApJL* 715 (2010) L133.
- [30] M. Gordovskyy, P.K. Browning, E.P. Kontar, N.H. Bian, Particle acceleration and transport in reconnecting twisted loops in a stratified atmosphere, *A&A* 561, 2014, 15pp.
- [31] G.H. Golub, J.M. Ortega, *Scientific computing and differential equations: an introduction to numerical methods*, Academic Press, London, 1992.
- [32] C.E. Gutiérrez, *The Monge-Ampère Equation*, Birkhäuser, Boston, 2001.
- [33] S. Haker, L. Zhu, A. Tannenbaum, S. Angenent, Optimal mass transport for registration and warping, *Int. J. Comp. Vis.* 60 (2004) 225-240.
- [34] Å.M. Janse, B.C. Low, E.N. Parker, Topological complexity and tangential discontinuity in magnetic fields, *Phys. Plasmas* 17 (2010) 092901.
- [35] C.T. Kelley, *Iterative methods for linear and nonlinear equations*, SIAM, Philadelphia, 1995.
- [36] B. Kliem, Y.N. Su, A.A. van Ballegooijen, E.E. DeLuca, Magnetohydrodynamic modeling of the solar eruption on 2010 April 8, *ApJ* 779 (2013) 18pp.
- [37] D.A. Knoll, D.E. Keyes: Jacobian-free Newton-Krylov methods: a survey of approaches and applications, *J. Comput. Phys.* 193 (2004) 357-397.
- [38] H. Lamb, *Hydrodynamics*; 6th edition, Dover, New York, 1945.
- [39] J.P. René Laprise, A. Plante: A class of semi-Lagrangian integrated-mass (SLIM) numerical transport algorithms, *Mon Wea Rev* 123 (1995) 553-565.
- [40] G. Loeper, F. Rapetti, Numerical solution of the Monge-Ampère equation by a Newton's algorithm, *C. R. Acad. Sci. Paris, Ser I.* 340 (2005) 319-224.
- [41] B.C. Low, Magnetic helicity in a two-flux partitioning of an ideal hydromagnetic fluid, *ApJ* 646 (2006) 1288-1302.

- [42] S. Maeyama, A. Ishizawa, T.-H. Watanabe, N. Nakajima, S. Tsuji-lio, H. Tsutsui, A hybrid method of semi-Lagrangian and additive semi-implicit Runge-Kutta schemes for gyrokinetic Vlasov simulations, *J. Comput. Phys.* 183 (2012) 1986-1992.
- [43] R.J. McCann, Polar factorization of maps on Riemannian manifolds, *Geom. Funct. Anal.* 11 (2001) 589-608.
- [44] H.K. Moffatt, The degree of knottedness of tangled vortex lines, *J Fluid Mech* 35 (1969) 117-129.
- [45] G. Monge, Mémoire sur la théorie des déblais et des remblais, *Histoire de l'Académie Royale des Sciences de Paris* (1781) 666-704.
- [46] J.M. Ottino, *The kinematics of mixing: stretching, chaos, and transport*, Cambridge University Press, Cambridge, 1989.
- [47] E.N. Parker, *Spontaneous current sheets in magnetic fields: with applications to stellar X-rays*, Oxford University Press, 1994.
- [48] E.N. Parker, Nanoflares and the solar X-ray corona, *ApJ* 330 (1988) 474-479.
- [49] A.V. Pogorelov, *Monge-Ampère equations of elliptic type*, Translated from the first Russian edition by F. Leo Boron with the assistance of Albert L. Rabenstein, C. Richard, and P. Bollinger, Noordhoff Ltd., Groningen, 1964.
- [50] P.L. Pritchett, C.C. Wu, Coalescence of magnetic islands, *Phys. Fluids* 22 (1979) 2140-2146.
- [51] J.M. Prusa, P.K. Smolarkiewicz, An all-scale anelastic model for geophysical flows: dynamic grid deformation, *J. Comput. Phys.* 190 (2003) 601-622.
- [52] É. Racine, P. Charbonneau, M. Ghizaru, A. Bouchat, P.K. Smolarkiewicz, On the mode of dynamo action in a global large-eddy simulation of solar convection, *ApJ* 735 (2011) 22pp.
- [53] A.F. Rappazzo, M. Velli, G. Einaudi, R.B. Dhalburg, Nonlinear dynamics of the Parker scenario for coronal heating, *ApJ* 677 (2008) 1348-1366.
- [54] C. Schär, P.K. Smolarkiewicz, A synchronous and iterative flux-correction formalism for coupled transport equations, *J. Comput. Phys.* 128 (1996) 101-120.
- [55] J. Schumacher, B. Kliem, Coalescence of magnetic islands including anomalous resistivity, *Phys. Plasma* 4 (1997) 3533-3543.
- [56] P.K. Smolarkiewicz, P. Charbonneau, EULAG, a computational model for multiscale flows: An MHD extension, *J. Comput. Phys.* 236 (2013) 608-623.
- [57] P.K. Smolarkiewicz, Multidimensional positive definite advection transport algorithm: An overview, *Int. J. Numer. Meth. Fluids* 50 (2005) 1123-1144.
- [58] P.K. Smolarkiewicz, J.A. Pudykiewicz, A class of semi- Lagrangian approximations for fluids, *J. Atmos. Sci.* 49 (1992) 2082-2096.

- [59] P.K. Smolarkiewicz, J.A. Grell, A class of monotone interpolation schemes, *J. Comput. Phys.* 101 (1992) 431-440.
- [60] A. Staniforth, N. Wood, Aspects of the dynamical core of a nonhydrostatic, deep-atmosphere, unified weather and climate-prediction model, *J. Comput. Phys.* 227 (2008) 3445-3464.
- [61] A. Staniforth, J. Côté, Semi-Lagrangian integration schemes for atmospheric models-A review, *Mon. Wea. Rev.* 119 (1991) 2206-2223.
- [62] J. Strain, Semi-Lagrangian methods for level set equations, *J. Comput. Phys.* 151 (1999) 498-533.
- [63] M. Sulman, J.F. Williams, R.D. Russell, Optimal mass transport for higher dimensional adaptive grid generation, *J. Comput. Phys.* 230 (2011) 3302-3330.
- [64] J. Urbas, On the second boundary value problem for equations of Monge-Ampère type, *J. Reine Angew. Math.* 487 (1997), 115-124.
- [65] S.J. Thomas, J.P. Hacker, P.K. Smolarkiewicz, Spectral preconditioners for Nonhydrostatic Atmospheric Models, *Mon. Wea. Rev.* 131 (2003) 2464-2478.
- [66] N.S. Trudinger, X.-J. Wang, On the second boundary value problem for Monge-Ampère type equations and optimal transportation, *Ann. Sc. Norm. Sup. Pisa Cl. Sci.* 8 (2009) 143-174.
- [67] C. Truesdell, *The mechanical foundations of elasticity and fluid dynamics*, Gordon & Breach, New York, 1966.
- [68] M. Ugai, Propagation of plasmoids generated by fast reconnection in the geomagnetic tail, *J. Atmos. Sol. Terr. Phys.* 99 (2013) 47-52.
- [69] Z. Wang, J. Yang, F. Stern, A simple and conservative operator-splitting semi-Lagrangian volume-of-fluid advection scheme, *J. Comput. Phys.* 231 (2012) 4981-4992.
- [70] D.B. Xiu, G.E. Karniadakis, A semi-Lagrangian high-order method for Navier-Stokes equations, *J. Comput. Phys.* 172 (2001) 658-684.
- [71] X. Yuan, S.C. Jardin, D.E. Keyes, Numerical simulation of four-field extended magnetohydrodynamics in dynamically adaptive curvilinear coordinates via Newton-Krylov-Schwarz, *J. Comput. Phys.* 231 (2012) 5822-5853.
- [72] M Zerroukat, N. Wood, A. Staniforth, A three-dimensional monotone and conservative semi-Lagrangian scheme (SLICE-3D) for transport problems, *Q.J.R. Meteorol. Soc.* 138 (2012) 1640-1651.
- [73] V. Zheligovsky, O. Pogdvigina, U. Frisch, The Monge-Ampère equation: Various forms and numerical solution, *J. Comput. Phys.* 229 (2010) 5043-5061.